

Basis for selective drug evasion of an aminoglycoside-resistance ribosomal RNA modification

Received: 26 November 2024

Accepted: 14 August 2025

Published online: 27 August 2025


Debayan Dey ^{1,5}, Jacob M. Mattingly ^{2,3,5}, Natalia Zelinskaya ¹,
Christine M. Dunham ^{2,4}  & Graeme L. Conn ^{1,4} 

Aminoglycosides disrupt the fidelity of bacterial protein synthesis, but their potent antibacterial activity is threatened by multiple resistance mechanisms, including methylation of their ribosomal RNA (rRNA) binding site. However, the impact of one such resistance-conferring methylation on N1 of helix 44 nucleotide A1408 (m¹A1408) is highly variable with some aminoglycosides retaining significant potency. Here, we examine bacterial susceptibility to diverse aminoglycosides, determine high-resolution electron cryomicroscopy structures of m¹A1408-modified 70S ribosome-aminoglycoside complexes, and perform molecular dynamics simulations to decipher the key determinants of such “resistance evasion.” Collectively, these analyses reveal how some aminoglycosides adapt their conformation to accommodate m¹A1408, including the roles of specific ring substituents, balancing ligand strain and maintaining favorable interactions, as well as interactions made by additional functional groups that compensate for those disrupted by the modification. This work provides design principles that can guide future rational development of aminoglycosides refractory to resistance conferred by rRNA modifications.

Aminoglycosides are broad-spectrum ribosome-targeting antibiotics with activity against both Gram-negative and Gram-positive bacteria^{1,2}. Currently, aminoglycosides are in clinical use as last-resort antibiotics for patients with severe or complicated infections (e.g., sepsis, infective endocarditis), including multidrug-resistant (MDR) Gram-negative infections, and for long-term treatment of chronic *Pseudomonas aeruginosa* lung infections associated with cystic fibrosis^{3,4}. Broader application has been limited by aminoglycoside toxicity relative to other treatment options, but increasing resistance to these other drug classes has led to a reevaluation of aminoglycoside use^{5–7}. However, continued use of aminoglycosides is also threatened by multiple resistance mechanisms, including efflux and chemical modification of either the drugs or their ribosomal binding site^{8–11}.

Aminoglycosides bind 16S rRNA helix 44 (h44) at the aminoacyl-tRNA site (A site) within the conserved decoding center of the bacterial ribosome and typically induce mRNA misreading to disrupt the fidelity of protein synthesis, eventually resulting in cell death¹. Aminoglycosides are polycationic oligosaccharides, with most containing a common 2-deoxystreptamine (2-DOS) ring (Ring II) appended with additional aminosugar rings (Fig. 1). The 2-DOS ring is connected at position 4 via a glycosidic bond to a modified α -glucose unit (Ring I) to form the disaccharide core that comprises the minimal fragment specifically able to bind to h44. Different classes of aminoglycosides are then distinguished based on the additional sugar linkages to the 2-DOS unit². A second modified α -glucose unit (Ring III) at position 6 of the 2-DOS ring forms the 4,6-DOS aminoglycosides, including

¹Department of Biochemistry, Emory University School of Medicine, Atlanta, GA, USA. ²Department of Chemistry, Emory University, Atlanta, GA, USA.

³Graduate Program in Biochemistry, Cell, and Developmental Biology (BCDB), Emory University, Atlanta, GA, USA. ⁴Emory Antibiotic Resistance Center (ARC), Emory University, Atlanta, Georgia, USA. ⁵These authors contributed equally: Debayan Dey, Jacob M. Mattingly.  e-mail: cmdunha@emory.edu; gconn@emory.edu

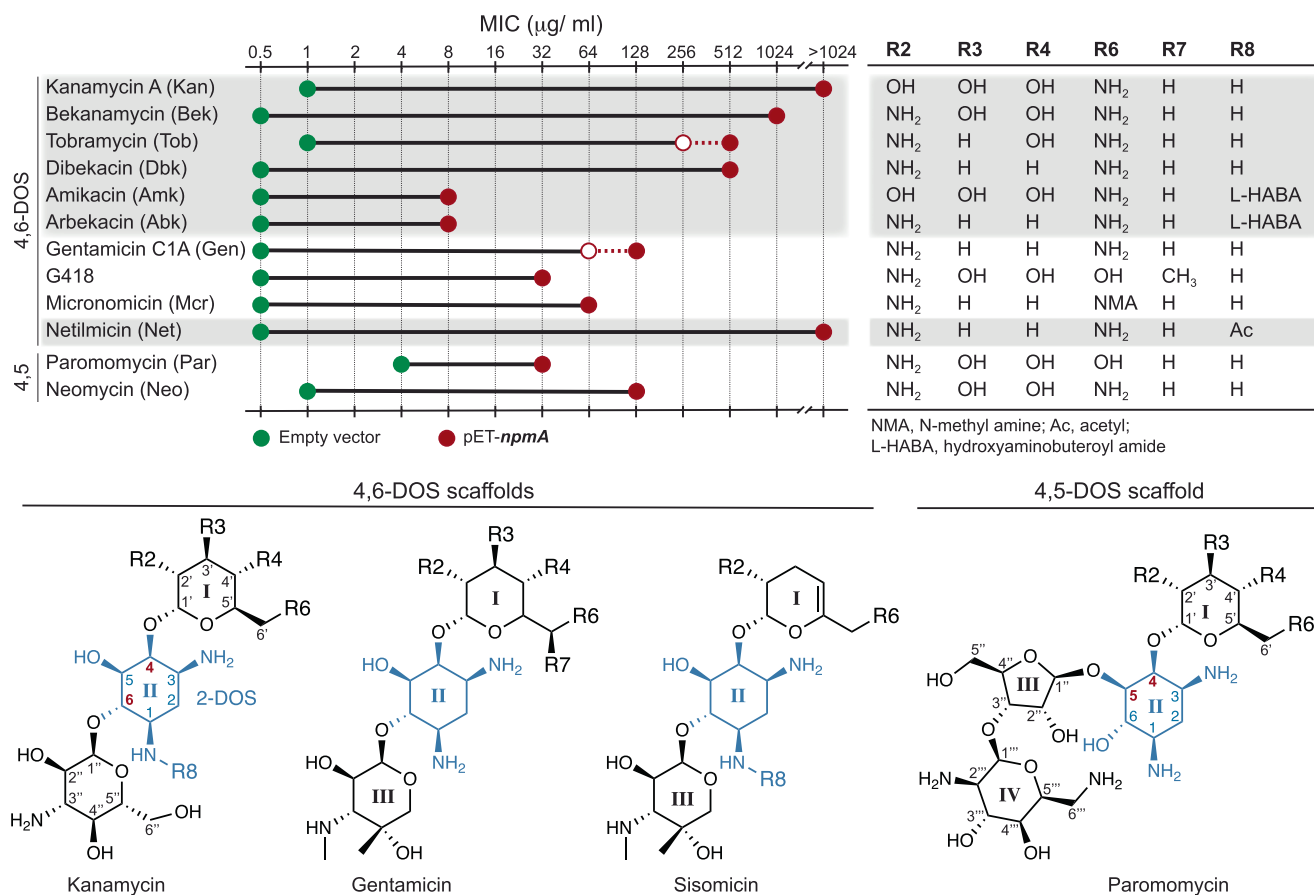


Fig. 1 | MICs of diverse aminoglycosides against *E. coli* with and without m¹A1408 modification. Structurally and chemically diverse aminoglycosides, including both 4,6- and 4,5-DOS drugs, were tested for their activity against *E. coli* without (green filled circles) and with (red filled and open circles) expression of NpmA, corresponding to the absence and presence of the m¹A1408 aminoglycoside-resistance modification, respectively. Where present, pairs of open

and filled circles denote a range for the final consensus MIC determined from the replicate measurements. Shaded regions denote aminoglycosides within the four chemical scaffolds shown below: kanamycin, gentamicin, sisomicin, and paromomycin. Individual substituents (R groups) in Rings I and II of these scaffolds are detailed in the accompanying panel (right).

kanamycin (Kan) and the clinically important drugs amikacin (Amk), tobramycin (Tob), gentamicin C1A (Gen), and plazomicin (Plz). Alternatively, appending the position 5 of the 2-DOS ring with a β -D-ribose moiety forms the scaffold of the 4,5-DOS class of aminoglycosides, including the trisaccharides ribostamycin and butirosin, tetrasaccharides neomycin (Neo) and paromomycin (Par; Fig. 1), and the pentasaccharide lividomycin.

Despite their potency and broad-spectrum activity, the emergence of aminoglycoside resistance among pathogenic bacteria has critically impacted the clinical efficacy of this drug class^{8–11}. Prevalent resistance mechanisms include efflux mediated by resistance-nodulation-division family transporters in Gram-negative bacteria, drug modification by aminoglycoside-modification enzymes (AMEs), and ribosomal drug binding site mutation or chemical modification by the aminoglycoside-resistance 16S rRNA methyltransferases^{9,11–13}. Countering the action of widespread AMEs has been the major focus of synthetic strategies to date, with alterations designed to restore aminoglycoside activity, such as in the recently approved Plz, which is based on the sisomicin scaffold^{14,15}. However, like established drugs of this class such as Tob and Amk, Plz—and likely future aminoglycoside variants developed using similar approaches—remain vulnerable to the action of aminoglycoside-resistance 16S rRNA methyltransferases, which have more recently emerged as another major clinical threat^{10,14}. These rRNA modification enzymes methylate either the N1 position of residue A1408 (m¹A1408; methyltransferases NpmA and NpmB) or the N7 position of G1405 (m⁷G1405; methyltransferases ArmA and RmtA to

RmtH) to render large groups of aminoglycosides ineffective^{12,13,16}. Members of the m⁷G1405 methyltransferase family have also been identified on plasmids encoding the NDM-1 β -lactamase, thus contributing to MDR in pathogenic bacteria, including *P. aeruginosa* and *Klebsiella pneumoniae*^{17,18}.

While m⁷G1405 and m¹A1408 confer near pan-aminoglycoside resistance, some aminoglycosides can, to varying extents, escape the effects of these two rRNA modifications. For example, the 4,5-DOS aminoglycosides are unaffected by m⁷G1405 as their Ring III does not project towards the modification site in this arrangement. Additionally, multiple reports of drug activity in bacteria expressing these enzymes have also suggested a propensity for certain aminoglycosides of both the 4,5-DOS and 4,6-DOS structural classes to partially evade the effect of the m¹A1408 modification^{13,19,20}. Further, Kanazawa et al.²¹ showed that G418 (also known as geneticin) and Par, both of which have a 6'-OH group, could bind to a model RNA helix that mimics the A site of the ribosome containing m¹A1408. In this context, the N1-methyl group of m¹A1408 and the 6'-OH group of Ring I of G418 and Par are close, suggesting better electrostatic and steric accommodation compared to Gen, which has a 6'-NH₃⁺ group.

Fully defining the basis for the differential impacts of resistance rRNA modifications on the activity of structurally similar aminoglycosides could yield critical insights to guide rational redesign of this drug class to fully evade the rRNA modification resistance mechanism. However, we currently lack the necessary understanding of the structural and dynamic attributes of aminoglycosides upon interaction

with modified, aminoglycoside-resistant ribosomes compared to their unmodified, fully drug-sensitive counterparts. Here, we develop an experimental and computational framework to provide such information to thereby define the mechanistic basis of evasion of m¹A1408-mediated resistance by specific aminoglycosides. We find that strong evasion requires a combination of favorable interactions of specific ring substituents, ring flexibility, and stabilization of drug-rRNA interaction by additional substituents such as the L-4-amino-2-hydroxybutyryl (L-HABA) moiety. Our studies also reveal why analogous evasion of the more clinically prevalent m⁷G1405 resistance modification is not observed and provide a platform from which new aminoglycoside-based drugs could be designed to fully evade rRNA modification-mediated aminoglycoside resistance.

Results

Aminoglycosides exhibit a range of susceptibilities to m¹A1408 rRNA methylation

Structurally and chemically diverse aminoglycosides were tested for activity in *Escherichia coli* using minimum inhibitory concentration (MIC) assays in the absence or presence of the m¹A1408 modification, i.e., without or with expression of the aminoglycoside-resistance methyltransferase NpmA, respectively. As anticipated based on prior observations with a more limited set of aminoglycosides^{13,19,20}, a wide range of changes in drug sensitivity are observed in the presence of the modification (MIC range from 8 to >1024 µg/ml) compared to unmodified ribosomes (MICs 0.5–1.0 µg/ml, except Par = 4 µg/ml), indicative of a range of capacities to evade resistance due to m¹A1408 (Fig. 1 and Supplementary Table 1). These differences must arise due to the distinct drug scaffolds, specific substituents presented on each ring, and/or their impact on the ability of a given aminoglycoside to adapt its ribosome-bound conformation to the presence of the methylated nucleobase of A1408.

The activities of some aminoglycosides based on the kanamycin scaffold are among the most strongly impacted by m¹A1408 modification: Kan, bekanamycin (Bek) and dibekacin (Dbk) are at least 1000-fold less effective with expression of NpmA (Fig. 1). Tob is also strongly impacted by the m¹A1408 modification but retains some activity (reduced 250- to 500-fold) compared to these three drugs. However, in sharp contrast, Amk and arbekacin (Abk), both of which have an L-HABA group attached to the 2-DOS ring (Ring II), exhibit strong retained activity against ribosomes with the m¹A1408 modification (MICs of 8 µg/ml compared to 0.5 µg/ml in the absence of NpmA; Fig. 1).

Aminoglycosides with a gentamicin scaffold, including Gen, micronomicin (Mcr), and G418, exhibit generally greater retained activity. Of these three drugs, G418, which uniquely has a 6'-OH in Ring I, shows the greatest ability to evade the impact of the m¹A1408 modification (Fig. 1). On the other hand, netilmicin (Net), an analog of sisomicin, which has a conformationally restricted Ring I, has the highest measurable MIC with NpmA expression (>1024 µg/ml; Fig. 1), highlighting a potential contribution of Ring I conformational flexibility to evasion of the m¹A1408 resistance modification.

Finally, for the two 4,5-DOS aminoglycosides tested, Neo and Par, distinct sensitivities to the m¹A1408 modification are again observed with a 16-fold difference in the impact of the resistance modification between the two drugs (Fig. 1). Neo and Par differ only in their Ring I 6' substituents (NH₃⁺ vs. OH, respectively) and, consistent with the observation for G418, these results suggest that the identity of the 6' substituent contributes significantly to the observed differences in sensitivity to m¹A1408.

Together, these results highlight the potential impacts of aminoglycoside features, including specific ring substituents, polarity, and ring flexibility, on drug sensitivity to m¹A1408-mediated aminoglycoside resistance. Additionally, these features encompass elements of aminoglycoside structure both near (e.g., Ring I substituents at the 6'

position) and distant from A1408 (e.g., addition of the L-HABA group to Ring II).

Structural basis for Abk and G418 evasion of the m¹A1408 aminoglycoside-resistance modification

To determine the structural basis for the ability of some aminoglycosides to strongly evade m¹A1408-mediated resistance, we determined electron cryomicroscopy (cryo-EM) structures of three *E. coli* 70S ribosome-drug complexes. For two aminoglycosides with distinct scaffolds and ring substituents that each exhibit retained activity in the presence of the m¹A1408 modification (Abk and G418), ribosome complexes were independently prepared and used to determine their structures bound to the m¹A1408-modified 70S ribosome (hereafter referred to as “70S (m¹A1408)”; Supplementary Figs. 1, 2, and Supplementary Table 2). The structure of the unmodified 70S (A1408)-Abk complex was also determined to enable direct comparison to the corresponding m¹A1408-containing structure (Supplementary Fig. 3 and Supplementary Table 2). Both 70S (m¹A1408)-drug complexes were prepared in the presence of mRNA and cognate tRNAs, while the 70S (A1408)-Abk complex lacked these ligands. The three final high-resolution cryo-EM maps, 70S (A1408)-Abk (2.7 Å), 70S (m¹A1408)-Abk (2.2 Å) and 70S (m¹A1408)-G418 (2.4 Å), show clear density corresponding to the bound aminoglycosides at the canonical location in the h44 ribosomal A site, permitting comparison of drug-ribosome interactions in the presence and absence of A1408 methylation (Fig. 2a–c and Supplementary Fig. 4). A distinct, secondary h44 binding site was also observed in all three structures one helical turn away from the canonical site. However, molecular dynamics (MD) simulations and the lack of activity of either drug in the presence of the m⁷G1405 modification at the canonical site indicate that this newly identified secondary site does not contribute meaningfully to ribosome inhibition (see Supplementary Fig. 5 and Supplementary Results for details).

Comparison of Abk bound to the ribosome with and without the m¹A1408 modification reveals discernible differences in aminoglycoside and adjacent rRNA nucleotide conformations, and their interactions (Fig. 2a, b and Supplementary Fig. 6a, b). In the modified rRNA, significant movement toward the phosphate backbone of A1493 of the Abk Ring I is necessary to avoid steric clash, while Rings II and III remain similarly anchored in both the modified and unmodified complexes. Local rRNA rearrangements, including changes in base pair and base step geometries near A1408, accommodate this shift with minimal more distant conformational impact on the A site. A recent structure of a 70S-Abk complex²² containing tRNAs and mRNA (PDB code 8IFC) also enabled a direct comparison with our empty 70S (A1408)-Abk complex lacking these RNA ligands. This comparison confirmed that the conformations of both Abk and its unmethylated rRNA binding pocket remain essentially unchanged regardless of the presence of tRNA and mRNA (Supplementary Fig. 6b). As such, differences in Abk observed between our empty 70S (A1408)-Abk and mRNA/tRNAs-bound 70S (m¹A1408)-Abk can be attributed exclusively to the presence of the modification on A1408.

In the 70S (A1408)-Abk complex, Abk engages with the phosphate backbone of 16S nucleotide A1493 and the nucleobases of G1494 and U1495 through its 2-DOS ring (Ring II), while the L-HABA group interacts with C1496 and G1497, and Ring III interacts with G1405 and C1407. The Ring I 6' substituent (NH₃⁺) is positioned to hydrogen bond with atom N1 of A1408 (2.6 Å distance) and is 4.9 Å from the phosphate backbone of A1493 (Supplementary Fig. 6b). Without any conformational adjustment of the rRNA or Abk, addition of the N1-methyl group to generate m¹A1408 would result in a clash with the Ring I 6'-NH₃⁺ (Fig. 2d, e). Thus, although many drug-rRNA interactions are retained in the 70S (m¹A1408)-Abk complex structure (Supplementary Table 3), the distance between the Abk Ring I 6'-NH₃⁺ and m¹A1408 N1 is increased from 2.6 to 5.3 Å (a 2.7 Å shift) due to A1408 methylation. Movements of both the m¹A1408 base (shifted by -1.5 Å and rotated

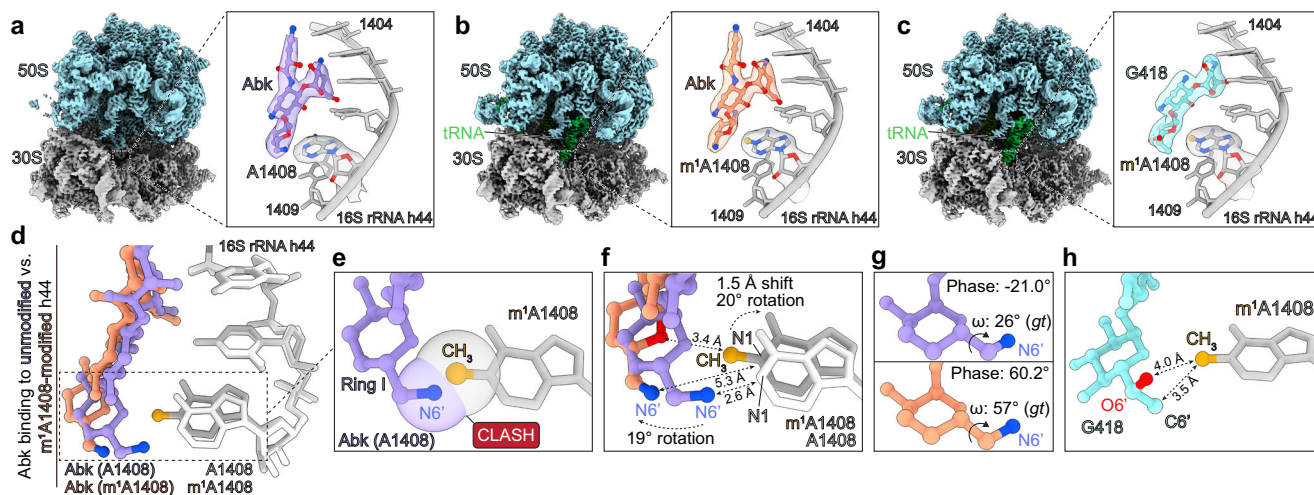


Fig. 2 | Structural basis for m¹A1408 modification-based resistance evasion.

a Cryo-EM map of the unmodified *E. coli* 70S ribosome-Abk complex (map threshold: 4.0; map value range -10.8 to 28.7) and a zoomed view (box) of Abk bound at the A site with map segments indicating positions of Abk and 16S nucleotide A1408 (map threshold 5.7). **b** Cryo-EM map of the m¹A1408-modified *E. coli* 70S ribosome-Abk complex (map threshold: 4.0; map value range -7.71 to 29.1) and a zoomed view (box) of Abk bound at the A site with map segments indicating positions of Abk and m¹A1408 (map threshold 5.1). **c** Cryo-EM map of the m¹A1408-modified *E. coli* 70S ribosome-G418 complex (map threshold: 4.0; map value range -7.98 to 28.5) and a zoomed view (box) of G418 bound at the A site with map segments indicating positions of G418 and m¹A1408 (map threshold 5.1).

d Superposition of the A-site rRNA nucleotides 1406–1408, comparing the unmodified (white) and m¹A1408-modified (gray) structures, showing conformational changes in Abk and m¹A1408. **e** The 6'-NH₃⁺ of Abk would clash with the m¹A1408 if it did not undergo a conformational change. **f** The glycosidic dihedral angle $\Phi_{I/II}$ rotates by 19° with a concurrent localized shift in the RNA conformation, moving m¹A1408 1.5 Å away with a 20° rotation of the base. **g** Comparison of Abk Ring I puckering when bound to the unmodified and m¹A1408-modified A site revealing changes in phase angle (-21° to 60°) and 6'-NH₃⁺ ω angle (26° to 57°). **h** G418 favorably positions its 6'-OH and CH₃ groups, 4.0 Å and 3.5 Å, respectively, from the methyl group of m¹A1408.

20°) and adjustment of the Ring I and II glycosidic bond orientation (dihedral angle $\Phi_{I/II}$ rotated by -19°) are necessary to accommodate the base methylation at A1408 (Fig. 2f, and Supplementary Fig. 6c and Supplementary Table 4). Other changes around A1408 include an increase in the distance between Abk Ring I O5' and N6 of A1408 from 3.6 to 5.4 Å, such that this interaction is disrupted when A1408 is methylated. Unique to the 70S (m¹A1408)-bound Abk, the methyl group of A1408 is oriented towards the Ring I O5' atom of Abk located 3.4 Å away and thus positioned to potentially make a weak C-H...O hydrogen bond (Fig. 2f and Supplementary Table 3). The Abk Ring I pucker also differs between the 70S (A1408)- and 70S (m¹A1408)-bound structures, with puckering phase angles of -21.0° and 60.2°, respectively; this change appears necessary to allow adjustment of the interatomic distance between the Ring I 6'-NH₃⁺ and N1 of A1408 (Fig. 2g and Supplementary Table 4). This change in ring pucker also alters the Ring I ω dihedral angle (O-C-C-6'-N/O, from 26° to 57°), though both remain closest to the *gauche/trans* (gt) configuration. Collectively, these changes in the glycosidic dihedral angles between Rings I and II, the ω dihedral angle, and the puckering phase angle of Ring I allow adaptation of Abk binding in the presence of the methyl group on m¹A1408.

Differences in RNA base step and base pair helical parameters and pseudo-torsional angles for base rotation are observed between the ribosome structures with unmethylated and methylated A1408. In the immediate vicinity of the bound Abk and m¹A1408, roll, twist and tilt angle differ for three consecutive base steps of 16S rRNA including C1407-A1408, A1408-C1409 and C1409-A1410, with additional changes in shift and slide for C1407-A1408 and A1408-C1409, respectively (Supplementary Fig. 6d). On the opposite strand, except for the unpaired and highly mobile nucleotides A1492 and A1493, no other base step parameters change significantly. Similarly, adjacent to A1408, changes in buckle, propeller twist, and opening angles are observed for base pairs C1407-G1494 and C1409-G1491, and base pair shear is also altered for C1407-G1494 (Supplementary Fig. 6e). Finally, pseudo-dihedral angles η'' and θ'' , which measure the twist and

bending in the RNA backbone, are most changed for nucleotides close to the modified m¹A1408 base (Supplementary Fig. 6f). These analyses reveal that conformational changes in the rRNA occur to accommodate binding of Abk when A1408 is modified, but that these changes are localized around m¹A1408 with no distant, large scale conformational changes being required. Comparison of the two 70S-Abk structures thus highlights the coordinated changes in both the drug conformation and locally within its rRNA binding site that are necessary to maintain interaction and effectively evade resistance conferred by m¹A1408.

Many analogous drug-RNA interactions are also observed in the 70S (m¹A1408)-G418 complex structure (Fig. 2c, h and Supplementary Table 4). However, as both the 3' and 4' positions of the G418 Ring I are substituted with a hydroxyl group, additional interactions are possible with the phosphate backbone of A1492. Additionally, in contrast to Abk, the 6' position of G418 has both 6'-OH and 7'-CH₃ groups which are positioned 4.0 Å and 3.5 Å from the methyl group of m¹A1408, respectively (Fig. 2h). The position of the 6'-OH is adjusted compared to a previously determined crystal structure of G418 bound to a model A-site RNA (PDB code 1MWL), in which it is oriented to hydrogen bond with atom N1 of A1408 (2.7 Å distant), with the 7'-CH₃ located 3.3 Å away from the N1 atom. Despite this reorientation of the G418 6'-OH, it is positioned closer to atom N1 of m¹A1408 compared to the 6'-NH₃⁺ of Abk (Supplementary Fig. 6b and Supplementary Table 3), which suggests the formation of a weak C-H...O hydrogen bond that might favor aminoglycosides like G418 containing a 6'-OH substituent. The G418 Ring I/II glycosidic linkage dihedral angles are intermediate between the values for Abk with A1408 vs. m¹A1408 for $\Phi_{I/II}$, and similar to both values for $\Phi_{I/II}$ (Supplementary Table 4). The G418 Ring I has a puckering phase angle of -5.7°, which is most similar to Abk bound to 70S (A1408) (Supplementary Table 4). These findings indicate that Abk, with its 6'-NH₃⁺, must move further from the partially charged m¹A1408 to avoid unfavorable interactions, necessitating a change in ring pucker that is not required for G418, for which smaller changes are necessary to adapt to the presence of the methyl group. Collectively,

these structures reveal key adaptations by specific aminoglycosides and their h44 binding site that allow them to maintain sufficient interaction with the rRNA to evade the impact of m¹A1408-mediated resistance.

Aminoglycoside conformational adaptation facilitates evasion of the m¹A1408 resistance modification

To fully define how evasion of m¹A1408 is achieved, a mechanistic analysis of a larger panel of aminoglycosides is needed, including those that evade resistance very poorly and for which empirical structural studies are therefore not possible. To accomplish this, we turned to all-atom MD simulations using a 25-nucleotide A-site rRNA model fragment (16S rRNA nucleotides C1403-U1414 and G1486-U1498; System 3), both with and without the m¹A1408 modification (hereafter referred to as modified and unmodified rRNA). Having established, as described above, that the presence or absence of tRNAs and mRNA does not significantly alter aminoglycoside conformation or the rRNA binding pocket, this simplified system was selected for computational efficiency and to take advantage of many available high-resolution experimental rRNA-aminoglycoside complex crystal structures determined using this model A-site RNA. Starting coordinates thus used these structures (where available) or were generated by docking based on the closest aminoglycoside structural analog, for a total of 12 different rRNA-aminoglycoside complexes (listed in Fig. 1 and Supplementary Table 1), with both unmodified and modified rRNA.

A partially restrained approach was used in which rRNA flexibility was limited by using a weak, empirically determined restraint (force constant, $k = 0.2 \text{ kcal/mol/\AA}^2$; see “Methods” for details). This approach was selected based on observations from the structural studies above, wherein the A-site rRNA exhibited comparatively smaller conformational changes than those of the aminoglycoside between unmodified and m¹A1408-modified ribosomes. Another consideration was to also avoid potential unrealistic binding scenarios that might arise from fully unrestrained simulation of the model rRNA in isolation. Each aminoglycoside was simulated bound to both modified and unmodified rRNAs in three 100 ns replicates, each following a 10 ns equilibration period, resulting in a total simulation period of 300 ns per aminoglycoside-rRNA complex. All simulations were assessed to ensure convergence of potential energy for the rRNA-aminoglycoside complex, convergence of aminoglycoside root mean square deviation (RMSD), and absence of major fluctuations in temperature or pressure during the production runs. To compare the rRNA-bound and free conformations of aminoglycosides, 100 ns MD simulations were also conducted for each aminoglycoside in its unbound state. Finally, conformational scanning with the Optimized Potentials for Liquid Simulations 4 (OPLS4) force field was used to systematically rotate glycosidic (Ring I/II) and ω dihedral angles in 10° increments for potential energy calculations to generate profiles corresponding to favorable (low energy) and unfavorable (high energy) conformations.

We first analyzed the Ring I/II dihedral angles ($\Phi_{I/II}$ and $\Psi_{I/II}$), and Ring I ω angle as these were observed to change in our structures for drugs able to evade the modification (Abk and G418; Fig. 2). $\Phi_{I/II}$ and $\Psi_{I/II}$ are continuously sampled in the simulations and do not show distinct clustering for the 11 tested aminoglycosides which remain stably bound to the modified A site during the simulation (Fig. 3a, b; note, as discussed further below, Net dissociated from its binding site in each of the three replicate simulations). In contrast, two distinct conformational clusters are observed for ω for aminoglycosides bound to modified rRNA (Fig. 3c). Conformational scanning of ω in free aminoglycosides (Kan, Bek, Tob and Dbk) reveals three energy minima corresponding to the *gt* (30 to 90°), *trans/gauche* (*tg*; 150 to 180° and -180 to -150°) and *gauche/gauche* (*gg*; -30 to -90°) conformations, with *gt* and *tg* being the most and least favorable, respectively (Supplementary Fig. 7a). In the simulations of rRNA-

bound aminoglycosides, the most favorable *gt* conformation is exclusively observed with unmodified rRNA, while distinct clusters of *gt* and *tg* conformations are predominantly observed when bound to modified rRNA (Fig. 3c). However, the adoption of each ω conformation when bound to modified rRNA depends upon distinct changes in $\Phi_{I/II}$ and $\Psi_{I/II}$ compared to the corresponding complexes with unmodified rRNA. We therefore refer to these distinct conformational states as “*gt* adaptation” and “*tg* adaptation,” reflecting the distinct structural adjustments required to accommodate the modified rRNA (Fig. 3d). In the *gt* adaptation, ω is maintained in the favorable *gt* conformation and changes in $\Phi_{I/II}$ and $\Psi_{I/II}$ are primarily responsible for the necessary movement of the Ring I 6' substituent (NH_3^+ or OH) away from the methyl group of m¹A1408 to minimize clashes. In contrast, in the *tg* adaptation, the major reorientation of ω is primarily responsible for moving the Ring I 6' group away from m¹A1408.

Comparison of *gt/tg* conformation populations when bound to modified rRNA reveals that the 4,6-DOS gentamicin scaffold aminoglycosides Mcr and G418, and the 4,5-DOS Par exhibit a higher prevalence of the energetically favorable *gt* adaptation compared to their close analogs Gen and Neo, respectively (Fig. 3e). These aminoglycosides also show smaller increases in MIC upon m¹A1408 modification suggesting that retained ability to bind modified rRNA in the *gt* conformation correlates with more effective evasion of the resistance modification (Fig. 1). Notably, unlike all the other aminoglycosides examined which possess a 6'- NH_3^+ group, Mcr, G418 and Par have either a 6'-OH (G418 and Par) or N-methylamine (6'- NH_2CH_3 ; Mcr) group. The predominance of the *gt* adaptation thus appears to be driven by electronic stabilization at the interface between Ring I and m¹A1408 (discussed further in the following section).

While the extent of *tg* adaptation appears to be a component of m¹A1408 evasion, this feature alone cannot explain all the observed differences in MIC changes between unmodified and modified ribosomes. For example, Kan exhibits a greater extent of *gt* adaptation (35%) compared to Bek (8%) (Fig. 3d), despite differing only in their Ring I 2' substituent, but still exhibits among the highest MICs with m¹A1408 modification (Fig. 1). Further, the activities of Amk and Abk are least impacted by the resistance modification, but these aminoglycosides do not exhibit a particularly high population of the *gt* adaptation when bound to the modified rRNA. Amk and Abk differ from two of the poorest evaders of the m¹A1408 modification, Kan and Dbk, respectively, by only the addition of an L-HABA group to Ring II. These observations suggest that additional factors beyond the polarity at the Ring I 6' position, such as the identity of other Ring I substituents or addition of the Ring II L-HABA moiety, also play a crucial role in determining the overall capacity for a given aminoglycoside to evade the m¹A1408 resistance modification.

Role of the Ring I 6' substituent on adaptation to the modified A site

To further explore how the polarity of the Ring I 6' substituent affects aminoglycoside conformation when bound to m¹A1408-modified rRNA, we compared the simulated conformations of three aminoglycosides of the gentamicin scaffold, Gen (6'- NH_3^+), Mcr (6'- NH_2CH_3) and G418 (6'-OH and 7'- CH_3), as well as the 4,5-DOS aminoglycosides Par (6'-OH) and Neo (6'- NH_3^+).

When bound to modified rRNA, the Gen Ring I is found in two populations corresponding to the *gt* (20%) and *tg* (80%) adaptations (Fig. 3d). As noted previously, these conformations require distinct shifts in $\Phi_{I/II}/\Psi_{I/II}$ compared to the favored *gt* conformation that is observed when bound to unmodified rRNA (Supplementary Table 5), and these shifts affect the positioning of the charged 6'- NH_3^+ group relative to the N1 of A1408. In the *gt* adaptation, rotations around $\Phi_{I/II}$ and $\Psi_{I/II}$ (11.1° and 5.1° , respectively) position the Gen 6'- NH_3^+ $\sim 5 \text{ \AA}$ from the N1 of A1408, placing the methyl group of m¹A1408 at a distance of $\sim 3.5 \text{ \AA}$, which is an energetically unfavorable arrangement (Fig. 4a). In

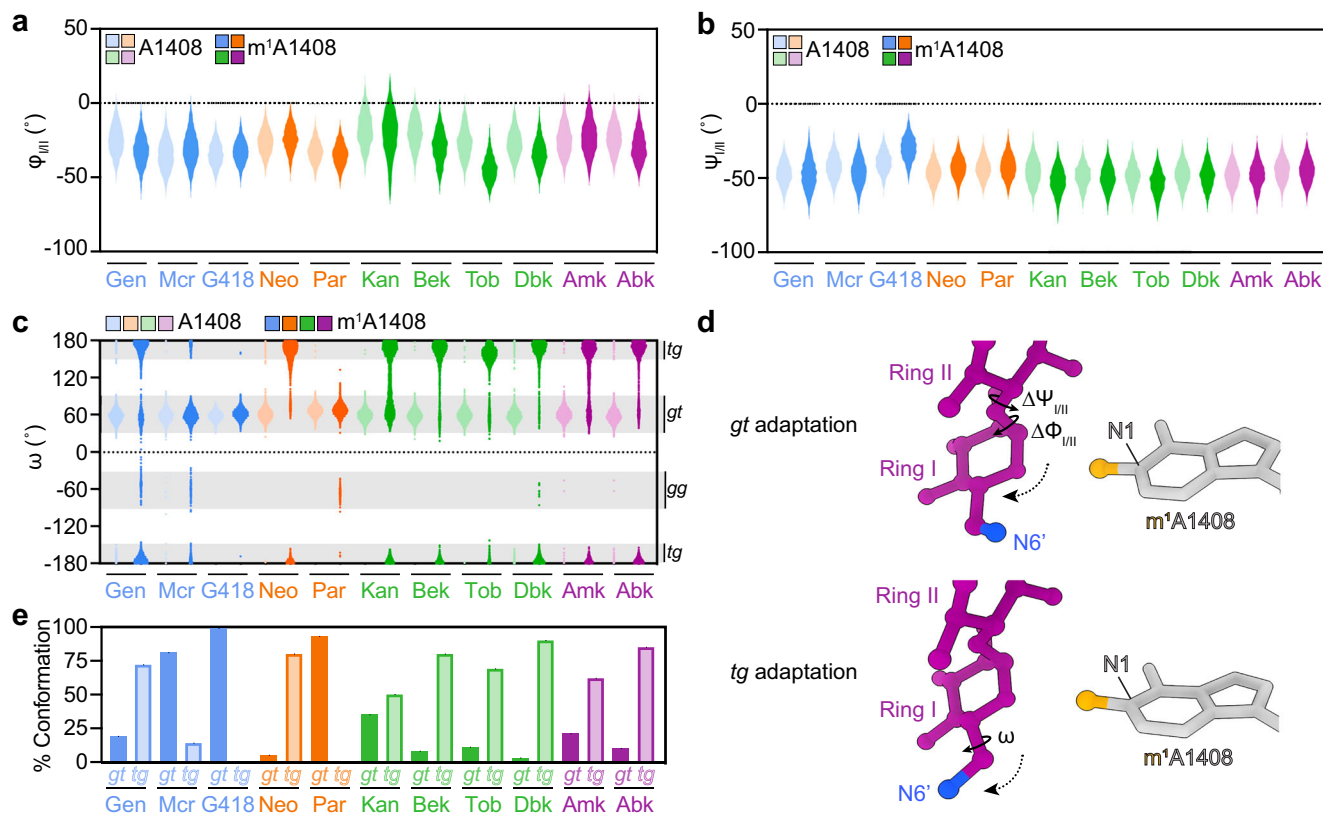


Fig. 3 | Aminoglycoside conformational adaptation facilitates evasion of the m¹A1408 resistance modification. **a** $\Phi_{1/II}$ and **b** $\Psi_{1/II}$ dihedral angle distributions from MD simulations (300 ns) of aminoglycosides bound to unmodified and m¹A1408-modified rRNA, indicating no distinct clustering in either case. Aminoglycosides are colored by scaffold: gentamicin (blue), paromomycin (orange), kanamycin (green), and kanamycin with L-HABA (purple). Lighter and darker shades represent binding to unmodified and m¹A1408-modified rRNA, respectively. **c** ω dihedral angle distribution, highlighting preferential clustering in the *gt*, *gg*, and

tg conformations (ranges shaded in gray). **d** Examples of *gt* and *tg* adaptations to the presence of m¹A1408 (shown for Amk), with the key rotations indicated around $\Phi_{1/II}/\Psi_{1/II}$ or ω , respectively. The resulting movements that position the N6' group further from the N1-methyl group in each case are denoted with the dotted line arrows. **e** Upon aminoglycoside binding to m¹A1408-modified rRNA, the population of conformations based on ω dihedral angle shows adaptations in the *gt* (dark shades) and *tg* (light shades) conformations.

contrast, the *tg* adaptation involves smaller rotations around $\Phi_{1/II}$ and $\Psi_{1/II}$ (6 and 2.6°, respectively; Fig. 4b) but positions the 6'-NH₃⁺ -6 Å from N1 of A1408 due to the additional rotation around ω , placing the methyl group of m¹A1408 at a distance of -5.2 Å. This difference also results in an overall average 6'-NH₃⁺-A1408 N1 interatomic distance of 6.7 Å when bound to the modified rRNA, as *tg* is the predominant conformation (Fig. 4c). As such, Gen can avoid making highly unfavorable interactions or clashes with the modification by predominantly adopting a less favorable *tg* conformation, which is necessitated by the presence of the NH₃⁺ group.

In contrast to Gen, Mcr has a 6' secondary amine with an additional 7'-methyl group and predominantly (~81%) binds to modified rRNA in the *gt* conformation (Fig. 3c, d and Supplementary Table 5). Small rotations around $\Phi_{1/II}/\Psi_{1/II}$ (both 3°) result in an average interatomic distance of -5 Å between the 6'-NH₃⁺ and N1 of A1408 and place the methyl group of m¹A1408 at a distance of -3.8 Å in the modified rRNA (Fig. 4c, d). The 7'-methyl group of Mcr and the methyl group of m¹A1408 are also -4.6 Å apart, placing them at a distance that can support favorable van der Waals interactions, likely stabilizing this interaction and making the *gt* adaptation more favorable in this context. The third gentamicin scaffold aminoglycoside, G418, binds to the modified rRNA almost exclusively in the more favorable *gt* conformation (~99%) attained through rotations about $\Phi_{1/II}$ and $\Psi_{1/II}$ of 1.5 and 9.1°, respectively, compared to its conformation when bound to unmodified rRNA (Figs. 3d, 4e). This adaptation places the Ring I 7'- and m¹A1408 methyl groups -4.0 Å apart and, similar to Mcr, positions

the 6'-OH and N1 of A1408 -5 Å apart, allowing more favorable interactions including a potential weak C-H...O hydrogen bond (Fig. 4e). Given that G418 and Mcr have identical Ring II and III structures, these differences in Ring I 6' substituent positioning, and the resultant interactions with the methyl group of m¹A1408, must give rise to the observed differences in MIC change (Gen > Mcr > G418; Fig. 1 and Supplementary Table 1) between bacteria with unmodified and modified rRNA.

Similar comparisons of the 6' substituents of Ring I are possible with Par and Neo, which have identical Ring I substituents except for their 6'-OH and 6'-NH₃⁺ groups, respectively. Neo primarily adopts a *tg* adaptation (~81%), with additional small adjustments in $\Phi_{1/II}$ and $\Psi_{1/II}$ (2.1 and 4.1°, respectively), resulting in a larger interatomic distance (>6 Å) between the 6'-NH₃⁺ and N1 of A1408 (Fig. 4c, f). In contrast, Par binds the modified rRNA exclusively in the more favorable *gt* conformation with only small adjustments of $\Phi_{1/II}/\Psi_{1/II}$ (2.3 and 1.2°, respectively) and maintaining an interatomic distance of -5 Å between the 6'-OH and N1 of A1408 (Fig. 4c, g and Supplementary Table 5). Again, the impact of m¹A1408 on activity (change in MIC: Neo > Par) must result from the relatively unfavorable versus favorable interactions made by the 6'-NH₃⁺ or 6'-OH substituent, respectively. Collectively, these findings highlight the important role of the 6' position in determining Ring I conformational preferences when binding to m¹A1408 and reveal that a 6'-OH facilitates better adaptation to the methylated target site and thus evasion of the resistance conferred by the modification.

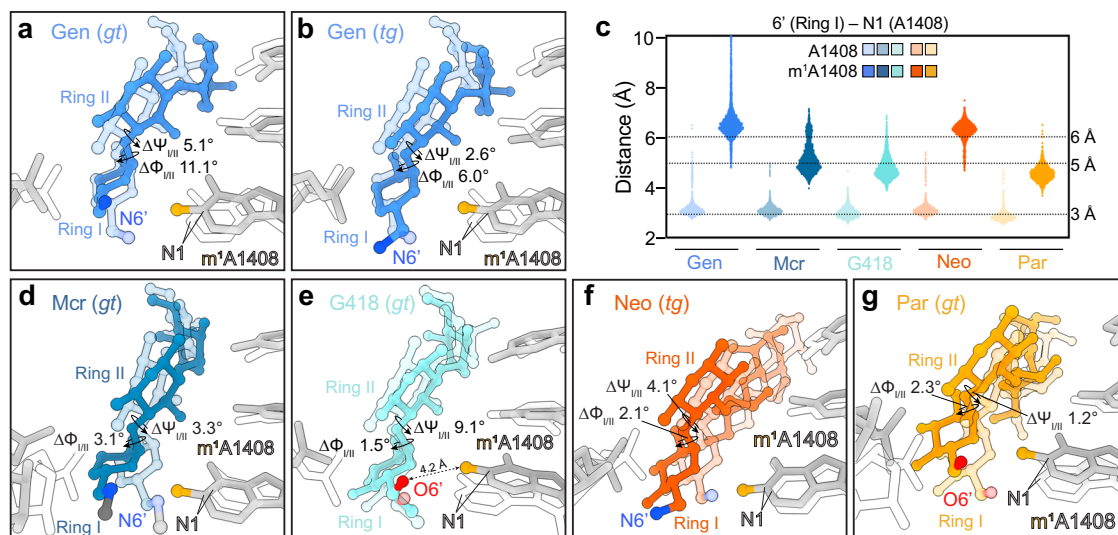


Fig. 4 | Role of the Ring I 6' substituent in adaptation to the modified A site. **a** Superposition of models of simulated Gen binding to m¹A1408-modified (opaque drug, gray RNA) or unmodified (semi-transparent drug, white RNA) 16S rRNA in the *gt* conformation. The $\Phi_{\text{I/II}}$ and $\Psi_{\text{I/II}}$ dihedral angles are shifted (Δ) in the presence of m¹A1408 compared to the unmodified base. **b** Superposition of models of simulated Gen binding to m¹A1408-modified or unmodified 16S rRNA in the *tg*

conformation. **c** Distribution of interatomic distances between the aminoglycoside 6' substituent and N1 of A1408, showing greater distances are necessary for accommodation of m¹A1408 by drugs with 6'-NH₃⁺ (Gen and Neo) compared to 6'-OH (Mcr, G418 and Par). Structural superposition of simulated A site-bound **d** Mcr (*gt* adaptation), **e** G418 (*gt* adaptation), **f** Neo (*tg* adaptation) and **g** Par (*tg* adaptation), with and without A1408 methylation.

Influence of other Ring I substituents on adaptation to the m¹A1408-modified A site

The four kanamycin scaffold aminoglycosides without a Ring II L-HABA group—Kan, Bek, Tob, and Dbk—share a common Ring I 6'-NH₃⁺ substituent but are otherwise distinct in terms of the number and polarity of their other Ring I substituents (Fig. 1 and Supplementary Fig. 7b), allowing us to explore the role of these substituents in resistance evasion. Kan and Bek exhibit a similarly low ability to evade the effect of m¹A1408 modification, with both exhibiting among the largest changes in MIC with NpmA expression (Fig. 1). The population of conformations corresponding to the *gt* adaptation in Kan (35%) and Bek (8%) differs, with rotations around $\Phi_{\text{I/II}}$ and $\Psi_{\text{I/II}}$ of 5.8° and 9.2° for Kan compared to 11.5° and 1.1° for Bek (Fig. 5a and Supplementary Table 5). These shifts position Ring I 6'-NH₃⁺ ~5 Å from the N1 of A1408 in both Kan and Bek (Fig. 5a, e). The more prevalent *tg* adaptations, Kan (50%) and Bek (80%), require larger shifts in $\Phi_{\text{I/II}}$ and $\Psi_{\text{I/II}}$ of 11° and 3.6° in Kan compared to 8.8° and 0.6° in Bek, but similarly position the Ring I 6'-NH₃⁺ group ~6.2 Å from A1408 for both aminoglycosides (Fig. 5b–e). However, despite the apparent greater capacity of Kan to adopt the *gt* adaptation and its greater flexibility around $\Psi_{\text{I/II}}$, it nonetheless fails to evade the resistance conferred by m¹A1408 with a change in MIC identical to Bek.

To assess the availability of conformations of Kan and Bek capable of binding to the ribosomal A site, we performed 100 ns MD simulations of the free states of these aminoglycosides. The $\Psi_{\text{I/II}}$ angle range for aminoglycosides is categorized into *syn-Ψ* (−30° to −90°) and *anti-Ψ* (150° to 180° and −150° to −180°). *Syn-Ψ* corresponds to the ribosomal A site-bound aminoglycoside conformation, whereas the *anti-Ψ* conformation is incompatible with binding to the A site²³. Kan exhibits two distinct clusters corresponding to *syn-Ψ* and *anti-Ψ* conformation angle ranges, while, in contrast, Bek is exclusively observed in the *syn-Ψ* conformation (Supplementary Fig. 7c,d). In the *syn-Ψ* conformation, the Kan 2'-OH and 5-OH of Ring II interact favorably (Fig. 5f), while in Bek a hydrogen bond forms between the 2'-NH₃⁺ and 5-OH of Ring II (Fig. 5g). In the *anti-Ψ* conformation, the Kan 2'-OH interacts favorably with a different Ring II substituent, 3-NH₃⁺ (Fig. 5h), whereas in Bek the *anti-Ψ* conformation results in electrostatic repulsion between 2'-NH₃⁺ and 3-NH₃⁺, making this conformation disallowed (Fig. 5i). We further

observed that Tob and Dbk also exclusively adopt a *syn-Ψ* conformation due to their 2'-NH₃⁺ (Supplementary Fig. 7d). These results are also consistent with previous MD simulations using NMR-derived time-averaged restraints of the Ring I/II disaccharide fragment of a more limited set of aminoglycosides and for a shorter time (5 ns) which showed adoption of both *syn-Ψ* and *anti-Ψ* for Kan but only *syn-Ψ* for Tob²³. Thus, the greater-than-expected sensitivity of Kan to m¹A1408 may be explained by its higher propensity to adopt a conformation (*anti-Ψ*) that is incompatible with binding to the A site without first converting to the *syn-Ψ* conformation. Such conversion of the “inactive” drug fraction in the free state may be less readily accomplished in the context of the less favorable interaction with the m¹A1408-modified A site.

Tob, Dbk and Bek exhibit a range of MIC changes upon m¹A1408 modification in the order Bek > Dbk > Tob (Fig. 1 and Supplementary Table 1). As these aminoglycosides have a common 2'-NH₃⁺ and differ only in the presence or absence of 3'-OH/4'-OH, they offer an opportunity to assess the impact of these additional Ring I substituents on adaptation to m¹A1408. We first compared the *tg* adaptations of Bek (3'-OH and 4'-OH), Tob (4'-OH only), and Dbk (no OH at either site), which are accomplished through $\Phi_{\text{I/II}}/\Psi_{\text{I/II}}$ changes of −9°/1°, −17°/5° and −6°/1°, respectively (Fig. 5c, d, j, k and Supplementary Table 5). The largest shifts are observed for Tob, allowing its 4'-OH group to reorient and interact with the phosphate backbone of A1492 (Fig. 5j). This new favorable interaction likely contributes significantly to its greatest ability among this group to evade the impact of the modification. In contrast, while Bek appears to exhibit a greater ability to change in $\Phi_{\text{I/II}}$ as compared to Dbk (i.e., Bek > Dbk), the order of activity in the presence of m¹A1408 is reversed (Dbk > Bek). However, from analysis of the dihedral energy landscape of these three free aminoglycosides, Dbk appears to have the greatest flexibility around $\Phi_{\text{I/II}}/\Psi_{\text{I/II}}$ (Supplementary Fig. 7e), consistent with the absence of both bulky Ring I 3'-OH and 4'-OH substituents. Thus, inherent flexibility around the Ring I dihedrals alone does not determine resistance evasion.

We next used RMSD-based clustering to select representative frames from the simulations of Bek, Tob, or Dbk bound to m¹A1408-modified rRNA for calculation of ligand strain energy using molecular mechanics-generalized Born surface area (MM-GBSA). This analysis revealed ligand strain energy in the order Bek > Tob > Dbk

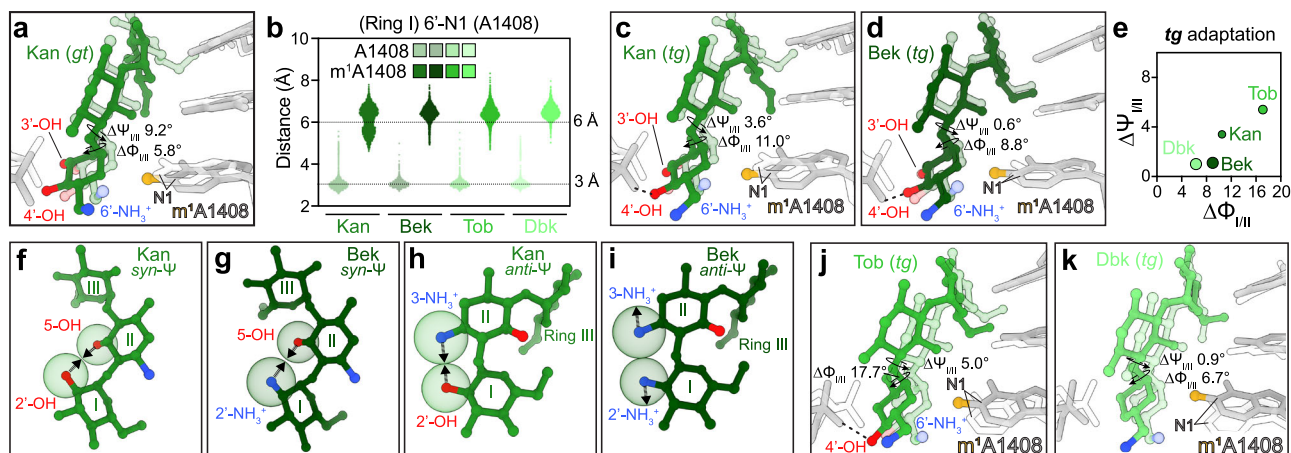


Fig. 5 | Influence of other Ring I substituents on adaptation to the m'A1408-modified A site. **a** Superposition of models of simulated Kan binding to m'A1408-modified (opaque drug, gray RNA) or unmodified (semi-transparent drug, white RNA) 16S rRNA in the *gt* conformation. The $\Phi_{I/II}$ and $\Psi_{I/II}$ dihedral angles are shifted (Δ) in the presence of m'A1408 compared to the unmodified base. **b** Distribution of interatomic distances between the 6'-NH₃⁺ of the kanamycin scaffold aminoglycosides and atom N1 of A1408 (with and without methylation), showing larger average distances compared to 6'-OH containing aminoglycosides (G418, Mcr, and Par; Fig. 4c), and suggesting unfavorable interactions with m'A1408. Superposition

of simulated A site-bound **c** Kan and **d** Bek in the *tg* adaptation. **e** Summary of shifts in $\Phi_{I/II}$ and $\Psi_{I/II}$ upon *tg* adaptation to m'A1408 for Kan, Bek, Tob and Dbk; circle size denotes the extent of *tg* adaptation. **f, g** *Syn-Ψ* and **h, i** *anti-Ψ* conformations of Kan and Bek, respectively. In the *syn-Ψ* conformation, Ring I and Ring II substituents of both Kan and Bek are positioned in a sterically and electrostatically favorable configuration. In contrast, in the *anti-Ψ* conformation, the repositioned Kan substituent interaction is favorable but unfavorable for Bek, resulting in a mixture of free drug configurations only for Kan. Structural superposition of simulated A site-bound **j** Tob and **k** Dbk in the *tg* adaptation.

(Supplementary Table 6), where higher strain energy in the bound state indicates a greater energetic cost of adaptation between the lowest-energy free and rRNA-bound states. Thus, the smaller change in $\Phi_{I/II}$ for Dbk results in lower strain (5.9 kcal/mol) compared to Bek, which experiences the highest strain of the three aminoglycosides (13.0 kcal/mol). Tob, which exhibits the largest $\Phi_{I/II}$ shift and additional change in $\Psi_{I/II}$, exhibits an intermediate strain (9.4 kcal/mol), and thus appears to achieve an optimal balance between minimizing steric hindrance and maintaining a favorable interaction via its 4'-OH. These trends are also reflected in the small change in time-averaged fractional rRNA-aminoglycoside hydrogen bond count calculated over the full 300 ns simulation for Tob (8.8 in unmodified rRNA vs. 8.5 in modified rRNA) compared to the more significant decreases for Dbk (7.9 to 6.4 hydrogen bonds) and Bek (9.7 to 8.7 hydrogen bonds), which indicate a loss of interaction energy that negatively impacts adaptability (Supplementary Table 7). Thus, while the absence of both 3'- and 4'-OH substituents results in lower ligand strain energy, Dbk lacks the ability to form interactions needed to adjust its glycosidic dihedral angles and engage with the rRNA phosphate backbone. Bek, despite having 3'- and 4'-OH groups, encounters high ligand strain energy and steric hindrances, making its interactions with the phosphate backbone unfavorable. In contrast, Tob, with only the 4'-OH substituent, exhibits greater flexibility to engage the phosphate backbone without incurring high strain energy, making it more adaptable to the modified rRNA.

Finally, when comparing MICs against modified rRNA, the sisomicin scaffold aminoglycoside Net exhibits a significantly higher value (>1024 µg/ml) compared to Dbk and Gen (Fig. 1 and Supplementary Fig. 8a). These three aminoglycosides have identical Ring I substituents, but Net differs in the presence of a carbon-carbon double bond in its Ring I. Our MD simulations reveal that after the 10 ns system equilibration, Net dissociates from the modified rRNA, likely due to unfavorable interactions, as indicated by the higher RMSD of Net compared to when bound to the unmodified rRNA (Supplementary Fig. 8a, b). In contrast, all other aminoglycosides remain bound throughout the 100 ns simulations. Conformational scans of $\Phi_{I/II}$ / $\Psi_{I/II}$ and ω for free Net and Gen reveal similar energetic landscapes and thus do not provide any insight into the basis for differences in MIC or behavior in the simulation (Supplementary Fig. 8c–e). However, a

severe restriction in Net Ring I pucker flexibility, resulting from the unsaturated carbon-carbon bond, was confirmed through a conformational scan of Ring I dihedral angles θ_3 and θ_4 , which revealed a narrower range of energetically favorable pucker angles for Net compared to Gen (Supplementary Fig. 8f, g). This restriction can explain the inability of Net to adapt to the modified RNA and highlights the additional crucial role of Ring I pucker in aminoglycoside adaptability, as observed in our structures of the 70S-Abk complexes.

Impact of Ring II L-HABA on aminoglycoside-rRNA interaction and resistance evasion

Amk and Abk have a kanamycin scaffold but are distinguished by the addition of an L-HABA group at their Ring II N1 position, which interacts with G1497, C1496, and U1495, thereby strengthening the A-site rRNA-drug interaction (Fig. 6a). Analysis of representative structures from RMSD-based clustering of these MD simulations reveals that the L-HABA group consistently maintains these interactions with the rRNA, regardless of the methylation status at A1408. The polar nature of the L-HABA group may also enhance the ability of Amk and Abk to engage in additional water-mediated interactions with the rRNA, unlike Kan and Dbk, which lack this group but are otherwise structurally identical. In the MD simulations, Amk and Abk maintain an average of 12.5 and 9.7 direct hydrogen bonds, respectively, with unmodified rRNA compared to 10.9 and 7.5 with modified rRNA (Supplementary Table 7). The overall greater number of direct hydrogen bonds and the potential water-mediated interactions of L-HABA with the A-site rRNA likely play a key role in the improved adaptability of Amk and Abk, allowing them to better overcome m'A1408-mediated resistance by enhancing binding to the modified rRNA.

Amk and Abk can both adopt either the *gt* or *tg* adaptation when binding to modified rRNA, with the latter being more prevalent (Fig. 6b). The differences in dihedral shifts and the populations of *gt* adaptations for aminoglycoside analogs with and without L-HABA, e.g., Amk (21%) compared to Kan (35%) and Abk (10%) compared to Dbk (3%), demonstrate that the presence of the L-HABA also influences *gt* adaptation. When bound to modified rRNA in either their *gt* or *tg* adaptation, Amk and Abk maintain a similar binding pose as observed with unmodified rRNA in the *gt* conformation, evidenced by the unchanged interatomic distances between these aminoglycosides and

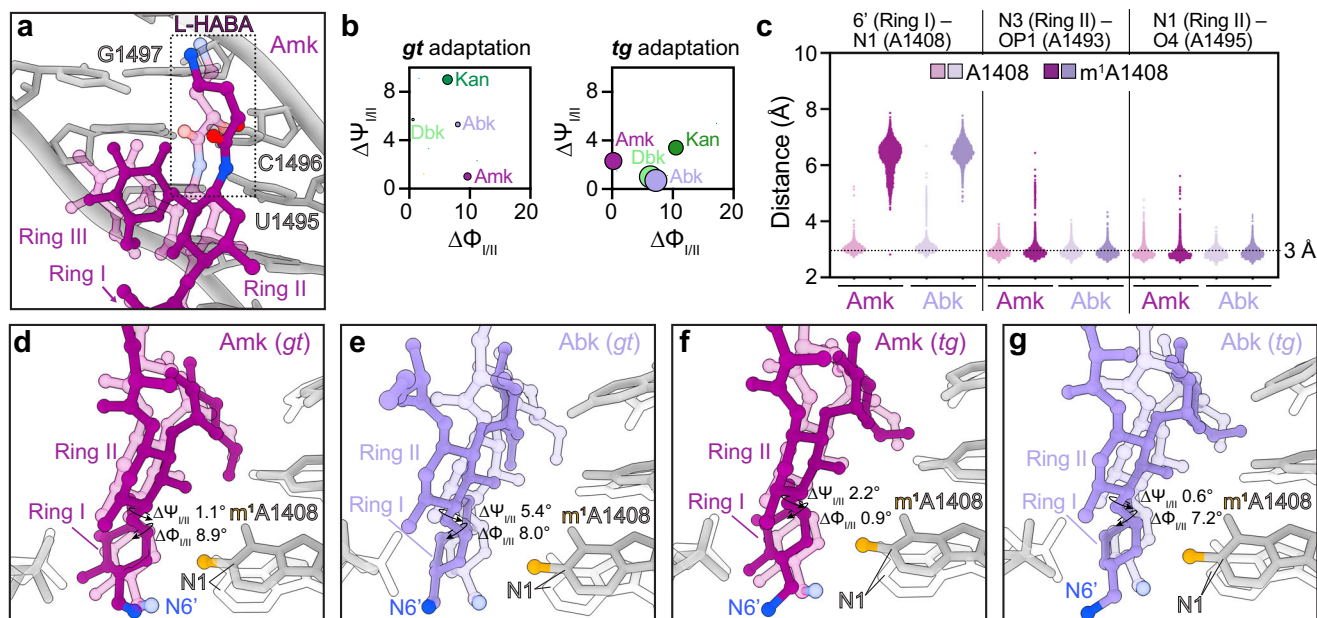


Fig. 6 | Impact of L-HABA on aminoglycoside-rRNA interaction. **a** Attachment of the L-HABA group to the 2-DOS ring (Ring II) establishes additional hydrogen bonds with the 16S rRNA distal to A1408, strengthening the interaction with the A site (shown for Amk). The L-HABA conformation remains stable, with the modification at A1408 not affecting its ability to interact with the RNA (opaque drug: m¹A1408; semi-transparent drug: unmodified A1408). **b** Differences in Φ_{III} and Ψ_{III} upon *gt* and *tg* adaptations for Amk and Abk compared to corresponding kanamycin scaffold aminoglycosides lacking an L-HABA group (Kan and Dbk, respectively).

Circle size denotes the extent of *gt* or *tg* adaptation. **c** Distribution of interatomic distances between the Ring I 6'-NH₃⁺ and N1 of A1408, and two rRNA contacts made by Ring II. For both Amk and Abk, changes in the 6'-NH₃⁺ to N1 distance are similar to other kanamycin scaffold aminoglycosides (Fig. 5b), which move away >6 Å due to the unfavorable 6' substituent. In contrast, the Ring II interactions are essentially unchanged upon m¹A1408 modification. Structural superposition of simulated A site-bound **d** Amk and **e** Abk in the *gt* conformation and **f** Amk and **g** Abk in the *tg* conformation.

Ring II during the simulations (Fig. 6c). Amk adopts the *gt* adaptation more frequently (21%) than Abk (10%) and smaller changes in the Amk Ring I dihedrals are required, particularly in Ψ_{III} , with Φ_{III}/Ψ_{III} changing by 8.9°/1.1° and 8.0°/5.4°, respectively, compared to their binding to unmodified rRNA (Fig. 6d, e and Supplementary Table 5). The differences in the 2'-OH/-NH₃⁺ groups also contribute to Amk's greater adaptability in the *gt* conformation compared to Abk, similar to what was noted above for Kan and Bek (Supplementary Table 5). In contrast, the *tg* adaptation requires shifts in Φ_{III}/Ψ_{III} 0.9°/2.2° and 7.2°/0.6° for Amk and Abk, respectively (Fig. 6f, g). These observations suggest that larger glycosidic dihedral changes are required in the *gt* adaptation to keep the 6'-NH₃⁺ (present in both Amk and Abk) and N1 of m¹A1408 at a distance of ~5 Å, while for the *tg* adaptation, a smaller shift is sufficient to more favorably position the two charges ~6 Å apart (Fig. 6b, d–g).

Plazomicin (Plz) is another clinically relevant L-HABA-containing aminoglycoside that is derived from the sisomicin scaffold. Plz differs from Net by the addition of this Ring II L-HABA and a hydroxyethyl modification of the Ring I 6'-amine (substituents R8 and R6, respectively, in Fig. 1). In contrast to Net, Plz remains stably bound to the m¹A1408-modified site during the simulation as indicated by its low RMSD throughout the trajectory (Supplementary Fig. 8h, i). This stability is likely facilitated by additional hydrogen bonding between the L-HABA group and rRNA, similar to that observed for Amk and Abk. Dihedral energy scans of free Plz also reveal comparable energetic preferences for both *tg* and *gt* ω -angle conformations (Supplementary Fig. 8j), a behavior that is reflected in its bound state: Plz samples both *tg* and *gt* conformations even at the unmodified A1408 site (Supplementary Fig. 8k). In the presence of the m¹A1408 modification, Plz predominantly adopts the *tg* adaptation. Although MIC data for Plz against methylated rRNA are not yet available, these results suggest that the presence of the L-HABA moiety and the 6'-secondary amine may confer increased conformational adaptability, potentially allowing Plz to partially evade m¹A1408-mediated resistance.

Collectively, these results reveal that the L-HABA group plays a crucial role in anchoring Amk, Abk, and potentially Plz to the rRNA by forming additional hydrogen bonds, which remain unaffected by the methylation of A1408. As such, these interactions substantially overcome penalties incurred due to other less favorable but necessary ring reorganizations or interactions with the modified base.

Role of aminoglycoside inherent flexibility in adaptation to modified RNA

Gen and Dbk have identical Ring I and II structures but differ in Ring III which influences the observed shifts in Ψ_{III} upon binding to modified rRNA (Supplementary Table 5) and results in greater *gt* adaptation for Gen (19%) compared to Dbk (3%) (Fig. 3d). Additionally, G418 exhibited a larger Ψ_{III} shift (9.1°) upon binding to modified rRNA compared to Gen (5.2°) and Mcr (3.3°) in the *gt* adaptation, despite sharing the same scaffold (Fig. 4a, d, e).

To understand the extent and impact of differences in inherent aminoglycoside flexibility around the Ring III/II dihedrals ($\Phi_{III/II}$) that may arise from variations in Ring III, we calculated the mean and standard deviation (SD) of aminoglycoside glycosidic dihedral angles in their free state from MD simulations (Supplementary Fig. 9a and Supplementary Table 8). Here, the dihedral angle SD serves as a proxy for flexibility at ring connections, with higher SD indicating greater flexibility. While $\Phi_{III/II}$ is comparatively rigid across all aminoglycosides, $\Psi_{III/II}$ exhibits substantial flexibility (Supplementary Fig. 9a and Supplementary Table 8). We next measured the dihedral angles of aminoglycosides when bound to unmodified and m¹A1408-modified rRNA and calculated the shifts in their mean values, revealing that aminoglycosides with a gentamicin scaffold exhibit greater shifts in $\Phi_{III/II}$ compared to those with a kanamycin scaffold (Supplementary Fig. 9b, c and Supplementary Tables 8, 9). This difference can likely be attributed to the absence of the 5' substituent in Ring III of the gentamicin scaffold, which enhances flexibility at this dihedral position. Notably, this increase in flexibility was most pronounced in G418

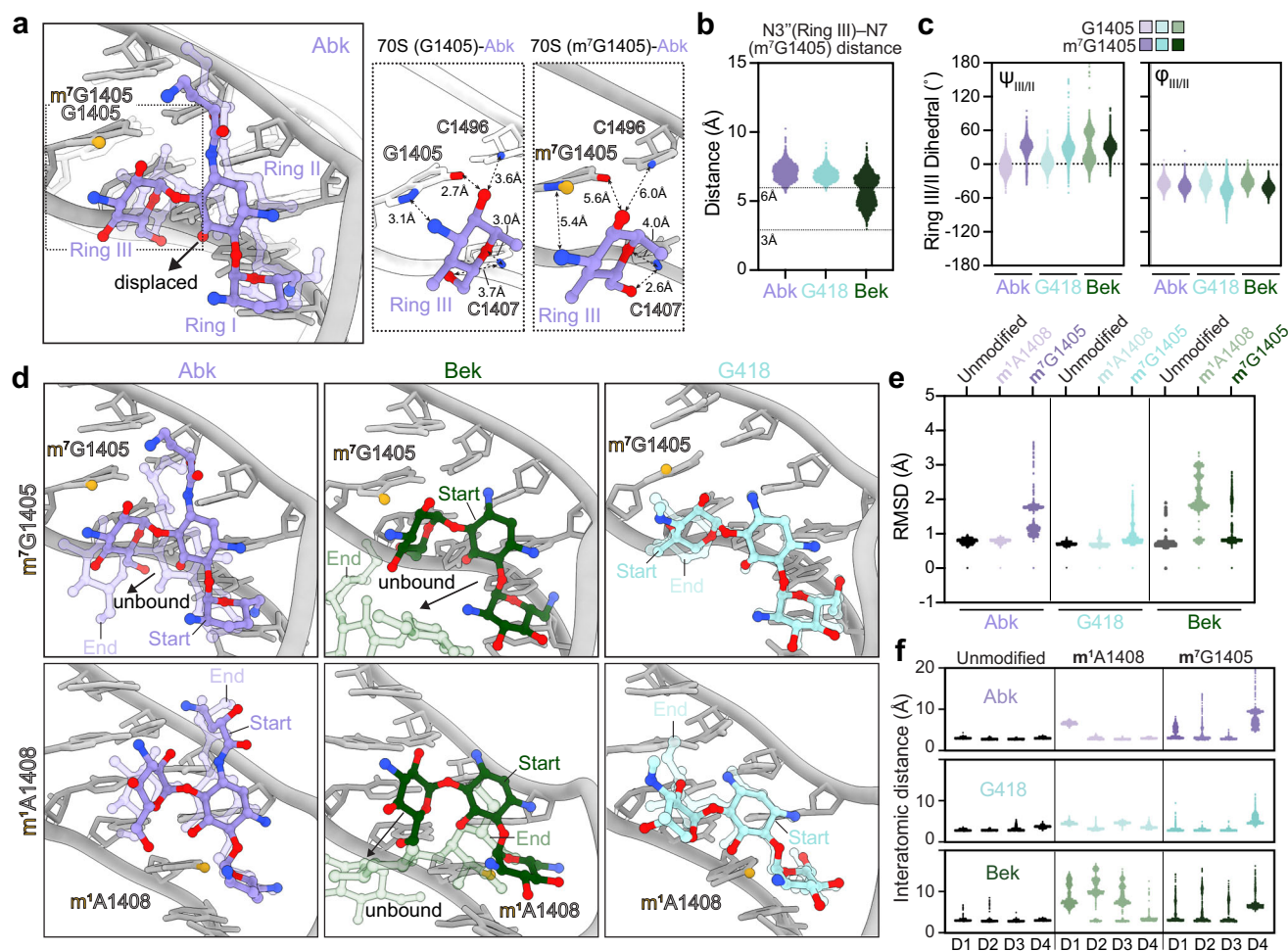


Fig. 7 | 4,6-DOS aminoglycosides fail to adapt to m⁷G1405-modified rRNA.

a Structural superposition of the initial models (prior to MD simulation) of Abk binding to m⁷G1405-modified (opaque drug, gray RNA) and unmodified (semi-transparent drug, white RNA) A-site rRNA. The indicated displacement of Abk from h44 by m⁷G1405 causes a loss of interactions between Abk and the rRNA, shown in the individual views (boxed region) of Ring III-rRNA contacts. **b** Interatomic distances between atom N7 of m⁷G1405 and the Ring III 3''-NH₃⁺ of Abk, G418, and Bek, from classical MD simulations are greater than 4 Å, precluding hydrogen bonding with G1405. **c** Dihedral angles at the Ring III/II glycosidic linkage of Abk, G418, and Bek bound to unmodified and m⁷G1405-modified rRNA from classical MD simulations. **d** Structural superpositions of unmodified, m¹A1408-modified and m⁷G1405-

modified A-site rRNA bound to Abk, G418, and Bek in REST simulations, showing unbinding events in Bek and Abk when simulated with a m⁷G1405-modified A site. **e** Aminoglycoside RMSDs in REST simulations show an increased range for Bek, G418, and Abk when rRNA is modified at m⁷G1405, with only Bek showing a similar increase when the rRNA is modified at m¹A1408. **f** Interatomic distance measurements—D1: N6' (Ring I)-N1(A1408), D2: N3 (Ring II)-OP1 (A1493), D3: N1 (Ring II)-O4 (U1495), and D4: N3'' (Ring III)-N7 (G1405)—reveal larger distance distributions for Bek, G418, and Abk when rRNA is modified at G1405, but only for Bek when rRNA is modified at m¹A1408, aligning with the observed changes in MICs in response to these resistance modifications.

(Supplementary Fig. 9b). We also observed that Abk exhibits greater changes in $\Phi_{III/II}$ compared to Amk (Supplementary Fig. 9b). This difference is likely due to the Abk Ring I 2'-NH₃⁺ group, which imposes greater conformational restrictions on $\Phi_{I/II}$ and $\Psi_{I/II}$ than for Amk (Supplementary Fig. 9a) and thus forces Abk to exploit alternative Ring III torsional adaptations in $\Phi_{III/II}$ and $\Psi_{III/II}$ to accommodate the m¹A1408 modification. Despite their comparable MIC values, this divergence highlights that even structurally similar aminoglycosides can evade resistance through distinct conformational adaptations. In addition, we found that the flexibility of $\Phi_{I/II}$ was generally more similar across the aminoglycosides, but $\Psi_{I/II}$ showed higher flexibility in Kan, Amk and G418 due to the presence of 2'-OH in Kan and Amk and 6'-OH in G418, further aiding in their adaptability.

4,6-DOS aminoglycosides fail to adapt to m⁷G1405-modified rRNA

In the absence of modification at G1405, Ring III of the 4,6-DOS aminoglycosides forms five interactions (hydrogen bonds and electrostatic

with nucleotides G1405, C1496, and C1407 (Fig. 7a). In contrast, 4,5-DOS aminoglycosides, with their distinct Ring III orientation, do not interact directly with G1405. Consistent with these previous structural observations, MIC analyses show that the activity of 4,5-DOS aminoglycosides is unaffected by m⁷G1405 methylation, whereas no 4,6-DOS aminoglycoside retains any significant activity (Supplementary Table 1). Using Bek, G418, and Abk as representative examples that reflect the range of abilities to evade the m¹A1408-mediated resistance based on their distinct ring structures (Fig. 1), we first modeled their complexes with A-site rRNA containing the m⁷G1405 modification. Maintaining fixed rRNA atoms and minimizing aminoglycoside conformations, we found that four of the five interactions with G1405, C1407 and C1496 are disrupted (shown for Abk in Fig. 7a).

We next conducted 100 ns MD simulations to explore why these aminoglycosides (Bek, G418, Abk) fail to effectively adapt their conformations in response to m⁷G1405. These MD simulations confirmed the loss of multiple Ring III interactions with rRNA, exemplified by the increased interatomic distance of ~6 Å between Ring III (N3'') and the

N7 atom of m⁷G1405. Loss of these interactions hinders effective binding and results in significant displacement of Abk, Bek and G418 from the binding pocket (Fig. 7b). Additionally, this Ring III movement results from changes in the glycosidic bond dihedral angles, particularly in $\Psi_{III/I}$ (Fig. 7c and Supplementary Table 10).

To capture binding and unbinding events that might not be readily accessible in classical MD due to ligand trapping in local energy minima, we applied replica exchange with solute tempering (REST) MD to rRNA complexes with these three aminoglycosides. REST MD enhances sampling by allowing replicas at different effective temperatures to exchange conformations, and thus increasing the potential to observe unbinding within the 100 ns simulation timescale²⁴. These simulations were conducted with Bek, Abk, and G418, bound to unmodified, m¹A1408-modified and m⁷G1405-modified rRNA. In the m¹A1408-modified rRNA complex, Bek exhibits unbinding events during the simulation, while in the presence of m⁷G1405, both Bek and Abk display similar unbinding behaviors (Fig. 7d). Further, while G418 does not exhibit a fully unbound state (Fig. 7d), substantial movement within the binding site is observed over the course of the simulation including partial displacement of Ring III (Fig. 7d). Consistent with maintained stable binding throughout the REST MD, lower RMSD values are observed for the aminoglycosides when bound with unmodified rRNA compared to those with modified rRNA (Fig. 7e). The RMSD values for aminoglycosides bound to m¹A1408-modified rRNA also accurately reflect the ability of each aminoglycoside to adapt to the modification: Abk exhibits the least variation in RMSD, indicating greater stability, while Bek showed the most variation, suggesting reduced stability with m¹A1408 (Fig. 7e). In contrast, simulations with m⁷G1405-modified rRNA show large RMSD fluctuations, indicating greater conformational changes in the aminoglycosides and instability of the complex (Fig. 7e). This observation is further supported by interatomic distance measurements, including Ring I (6')-A1408 (N1), Ring II (N3)-A1492 (OP2), Ring II (N1)-U1495 (O4), and Ring III (N3')-G1405 (N7) (Fig. 7f; denoted as distances D1 to D4, respectively). All these distances show increased fluctuations and shifts in the mean in complexes with m⁷G1405-modified rRNA, further illustrating the absence of an energetically plausible conformation for effective adaptation and thus explaining their failure to evade m⁷G1405.

Discussion

Aminoglycosides have been crucial as last-resort antibiotics, particularly in treating serious MDR infections^{2,7}. Resistance mechanisms, including AMEs, efflux pumps, and the methylation of rRNA residues A1408 and G1405, lead to pan-aminoglycoside resistance and are increasingly associated with MDR infections^{17,18}. Newer aminoglycosides like Plz can circumvent resistance from AMEs but remain vulnerable to rRNA methylation^{14,15,25,26}. However, while the effects of one of these resistance methylations (m¹A1408) was previously observed to be at least partly aminoglycoside-specific¹³, how ring substituents and inter-ring flexibility contribute to the greater ability of some drugs to evade the impact of methylation at A1408 remained unclear until the present work.

Using a diverse panel of aminoglycosides, we confirmed that the m¹A1408 modification leads to varied changes in *E. coli* susceptibility, with some drugs largely evading its effects. In contrast, the m⁷G1405 modification causes pan-resistance to 4,6-DOS aminoglycosides while 4,5-DOS aminoglycosides remain unaffected as they do not interact with G1405. This observation also indicates that there are no significant structural or allosteric alterations of aminoglycoside binding arising from m⁷G1405 modification. Additionally, the high resistance conferred by m⁷G1405 to 4,6-DOS aminoglycosides suggests that binding of these drugs at secondary sites, such as on the 50S ribosomal subunit or the second h44 site identified in our structures, does not contribute significantly to their antimicrobial activity despite observed impacts on ribosome function²⁷.

Our cryo-EM structures revealed that Abk and G418 binding to m¹A1408-methylated 70S ribosomes induces localized 16S rRNA conformational changes within two nucleotides of A1408, with more distant rRNA regions being essentially unchanged. Abk adapts by significantly altering its Ring I/II glycosidic dihedral angle to avoid the methyl group at A1408. Our results build on recent findings that a preorganized binding conformation is key to the effectiveness of bridged macrobicyclic antibiotics like cresomycin²⁸. When cresomycin binds to methylated ribosomes, the dimethylated nucleobase A2503 (m²m⁸A2503) shifts minimally (0.6 Å compared to its position in the ribosome unmodified at this site), while cresomycin adapts to the modification by undergoing a 14° dihedral angle change. This structural adjustment highlights a common adaptive strategy employed by antibiotics to overcome the challenges posed by methylated rRNA. While prior MD studies have assessed the conformational flexibility of aminoglycosides in their free state, including Neo, Kan, Amk and Tob^{23,29}, our studies additionally explored how these dynamics influence their adaptation to methylated RNA, revealing critical insights into resistance evasion.

Interestingly, while our simulations suggest that aminoglycosides containing a Ring I 6'-NH₃⁺ group can adapt to m¹A1408 by orienting this substituent in either the *gt* or *tg* configuration, with preference for *tg* adaptation, we observe only the *gt* adaptation via cryo-EM. MD simulations conducted with and without tRNAs and mRNA (Systems 2 and 3) revealed minimal impact of these ligands on the local dynamics of h44, suggesting that their presence does not significantly alter the conformational landscape of aminoglycoside binding. Further, similar distributions of *gt* and *tg* adaptations were observed in simulations using these larger systems and thus do not result from the minimal model system (System 3) used or the absence of other ligands such as tRNAs. The dominant *tg* conformation of Abk in the m¹A1408-modified A site thus likely reflects subtle energetic preferences, including electrostatic repulsion between the positively charged N1 of m¹A1408 and the N6' of Abk, as captured by the OPLS4 forcefield. Additionally, differences in buffer composition and temperature between cryo-EM and the MD simulation environment could contribute to the observed conformational variability between the two approaches. We emphasize, however, that our cryo-EM data empirically demonstrate aminoglycoside conformations that permit evasion of m¹A1408, while our MD simulations additionally permit exploration of drug conformations that may be shorter-lived or less energetically favorable and hence less likely to be observed in structural snapshots from cryo-EM.

The present work provides insight into the roles of specific aminoglycoside features in m¹A1408 resistance evasion, as well as the corresponding failure of any 4,6-DOS aminoglycoside to evade the resistance conferred by m⁷G1405. These key insights include:

1. Aminoglycosides containing a 6'-OH group (G418 and Par) or a 6'-secondary amine with a terminal methyl group (Mcr) show smaller changes in MIC between unmodified and modified rRNA. MD simulations revealed that these aminoglycosides bind more frequently to the modified A site in the *gt* conformation, with the proximity (~5 Å) between the Ring I 6'-position and N1 of A1408 indicating energetic favorability.
2. A 2'-OH group on Ring I (Kan) promotes adoption of a Ring I/Ring II *anti*- Ψ conformation in the free state, which is incompatible with binding to the A site and thus results in a fraction of the drug being "inactive" without conversion to *syn*- Ψ , which may be less favored in the presence of m¹A1408 modification.
3. The absence in Dbk of Ring I 3'- and 4'-OH groups reduces ligand strain energy upon 16S rRNA binding but limits crucial interactions with the rRNA phosphate backbone, resulting in fewer hydrogen bonds. In contrast, the presence in Bek of both 3'- and 4'-OH substituents leads to increased strain and steric hindrance, making interactions less favorable. The presence of only a 4'-OH achieves a balance of greater flexibility for engaging the backbone

- without high strain energy, resulting in the enhanced evasion of m¹A1408 observed for Tob.
- Consistent with recent studies showing that Abk exhibits prolonged association with the A site^{30,31}, addition of an L-HABA group to Ring II anchors Amk and Abk to the rRNA with three hydrogen bonds that are unaffected by m¹A1408 methylation, allowing significantly better resistance evasion compared to their non-L-HABA-containing analogs Kan and Dbk, respectively.
 - The loss of the Ring III 5' substituent in the gentamicin scaffold increases flexibility at the Ring III/Ring II glycosidic torsion that aids in adaptation to m¹A1408-methylated rRNA in the A site.
 - In the m⁷G1405-methylated A site, 4,6-DOS aminoglycosides require larger, unfavorable changes in their $\Phi_{III/II}$ and $\Psi_{III/II}$ torsions, potentially increasing ligand strain and leading to the loss of crucial hydrogen bonding interactions, which hinders effective adaptation to the A site.

These determinants, which can explain the observed differences in MIC between unmodified and m¹A1408- or m⁷G1405-modified rRNA, could be leveraged for structure-guided aminoglycoside design. By using smaller rRNA-aminoglycoside complexes for computational screening and optimization, this framework can also aid in understanding other resistance mechanisms or toxicity arising from aminoglycosides binding to eukaryotic ribosomes. This approach could thus accelerate the discovery of new aminoglycoside analogs with lower toxicity and improved resistance evasion, providing valuable antibiotics for treating Gram-negative and mycobacterial infections. Overall, this work provides a structural and computational framework for understanding adaptations to modified binding sites, such as rRNA methylation, that can be broadly applied to other antibiotics, accounting for the dynamics of both the free antibiotic and its complex with the binding site, shaped by substituents and structural features. This framework can thus elucidate antibiotic resistance mechanisms and serve as a computational tool for structure-activity relationship studies in future antibiotic design.

Methods

Antibiotic minimum inhibitory concentration (MIC) measurements

Antibiotics were purchased from Alfa Aesar (Mcr, J66072; Tob, J66040; and Neo, J61499), AstaTech Inc. (Net, 42439), BOC Sciences (Abk, 51025-85-5 and Dbk, 34493-98-6), Chem-Impex (Amk, 01693 and Par, 01507), Sigma (Bek, B5264), Teknova (G418, G5001) and Toku-E (Gen CIA, 26098-04-4). Fresh cation-adjusted Mueller–Hinton (CA-MHB; Sigma, 70192) medium (5 ml) containing 100 µg/ml ampicillin (Gold Biotechnology Inc, A-301-100) was inoculated (1:100 dilution) with saturated overnight culture of *E. coli* BL21(DE3) harboring plasmid encoding NpmA (pET-*npmA*), RmtB (pET-*rmtB*), or empty pET-44 control. Generation of these protein expression plasmids for NpmA (UniProt A8C927) and RmtB (UniProt Q76G15) using gene synthesis with *E. coli* codon optimization was described previously^{12,32,33}. All cultures were grown to ~0.1 A₆₀₀ at 37 °C with vigorous shaking. Cells from 1 ml of culture were collected by centrifugation, washed with phosphate-buffered saline solution (2 × 0.5 ml), and resuspended CA-MHB medium to 0.1 A₆₀₀ (5 × 10⁷ cfu/ml). Following 50× further dilution with CA-MHB, 100 µl of diluted culture (1 × 10⁵ cfu/well) was used to inoculate an equal volume of CA-MHB medium, pre-dispensed on a 96-well plate, containing 10 µM isopropyl β-D-thiogalactopyranoside (Gold Biotechnology Inc., I2481C) and a range of antibiotic concentrations. For cells with pET-*npmA* or pET-*rmtB*, an antibiotic concentration range of 2–1024 µg/ml was tested, except for Abk with pET-*npmA* for which 0.06–32 µg/ml was used. For empty pET-44 control, a range of 0.06–32 µg/ml was tested. MIC measurements were made in technical duplicates using two independent bacterial transformations for each plasmid/drug combination. Wells with no

antibiotic or no cells served as additional controls for each set of replicates. The plates were incubated at 37 °C with shaking and A₆₀₀ measurements taken after 24 h. The MIC was defined as the lowest concentration of antibiotic that inhibited growth, i.e., A₆₀₀ of <0.05 above background.

Ribosome purification and 70S complex assembly

Expression of NpmA from pET-*npmA* was used to obtain modified *E. coli* 70S (m¹A1408) ribosomes using 50 µM isopropyl β-D-thiogalactopyranoside (10× the concentration used for MIC measurements). 70S ribosomes, with and without NpmA modification, were purified identically and as previously described^{34,35}. 30S subunits isolated from 70S (m¹A1408) could not be further modified by purified NpmA in an in vitro methylation assay (<0.3% activity compared to unmodified 30S subunit), confirming high-level modification of A1408 in these ribosomes. 70S (A1408) ribosome-Abk complex was prepared by incubating purified *E. coli* 70S ribosomes (0.5 µM) with Abk (0.5 mM) in Buffer 2 (10 mM HEPES/KOH pH 7.6, 10 mM MgCl₂, 100 mM NH₄Cl and 6 mM 2-mercaptoethanol) at 37 °C for 40 min. Following incubation, 70S complexes were briefly placed on ice until used to prepare grids for cryo-EM. Aminoglycoside complexes with NpmA-modified ribosomes were assembled by incubating purified 70S (m¹A1408) (0.75 µM) with in vitro transcribed mRNA (2.5 µM; P- and A-site sequence: AUG GUA) and aminoglycoside (1 mM; Abk or G418) at 37 °C for 20 min. Purified *E. coli* tRNA^{Met} and tRNA^{Val} (2.5 µM) were added and the final complex incubated at 37 °C for an additional 20 min before briefly placing on ice until used to prepare grids for cryo-EM.

Cryo-EM structure determination

Specimen preparation. To prepare samples for cryo-EM, C-Flat™ holey carbon gold grids (R1.2/L3, 300 mesh; Electron Microscopy Sciences) were glow discharged in a PELCO easiGlow™ glow discharger (Ted Pella) for 15 s. Grids were prepared in a VitroBot Mark IV (FEI) at 4 °C and 100% humidity. 70S complex (3 µl) was applied to the grid and allowed to stand for 15 s before blotting for 4 s (for the 70S (A1408)-Abk complex) or 3.5 s (for both 70S (m¹A1408) complexes) and plunging into liquid ethane to vitrify. Prepared grids were stored under liquid nitrogen until performing quality screens and data collection.

Cryo-EM data collection. Cryo-EM data were collected for 70S (A1408)-Abk (17,071 micrographs), 70S (m¹A1408)-Abk (5053 micrographs) and 70S (m¹A1408)-G418 (5302 micrographs) at the National Center for CryoEM Access and Training (NCCAT) using a Krios G3i (Thermo Fisher Scientific) cryo-transmission electron microscope operating at 300 kV. Movies for the 70S (A1408)-Abk complex were recorded with a total electron dose of 52 e[−]/Å² and magnification of 81,000× (pixel size of 1.069 Å/px) using a Gatan K3 direct electron detector. Movies for the 70S (m¹A1408)-Abk and 70S (m¹A1408)-G418 complexes were recorded with a total electron dose of 50 e[−]/Å² and magnification of 96,000× (pixel size of 0.814 Å/px) using a Thermo Fisher Scientific Falcon 4i direct electron detector.

Image processing. Prior to processing cryo-EM data, movie frames were aligned using motion correction in RELION-3.1³⁶, and contrast transfer function (CTF) parameters were estimated for the motion-corrected micrographs using GCTF³⁷. Micrographs displaying poorer than 3 Å (70S (A1408)-Abk) or 6 Å (both 70S (m¹A1408) datasets) estimated maximum resolution were discarded. Following pre-processing, an initial round of automated particle picking was performed on a random subset of 50 micrographs using the reference-free Laplacian-of-Gaussian autopicker in RELION. Particles were extracted and downsampled by a factor of 4, then subjected to a round of reference-free two-dimensional classification in RELION-3.1 to generate 2D reference images, which were then used to perform

reference-based automated particle picking on the random micrograph subsets. Picked particles were extracted, 2D-classified, and manually curated to remove junk particles and particles picked on carbon, then used to train a Topaz particle picking model³⁸, which was used to pick particles from all retained micrographs in each dataset. Identified particles were extracted from micrographs with 4× down-sampling and subjected to 2D classification. Non-ribosome-like 2D classes were discarded.

Following identification of ribosome-like particles, initial 3D reconstructions were generated for each dataset in RELION-3.1 using the stochastic gradient descent method³⁹. Initial reconstructions were checked to ensure correct handedness before performing three-dimensional classification with particle alignment to identify 70S ribosome particles. Particles in non-70S classes (including junk classes and 50S ribosomal subunits) were discarded. Following 3D classification, particles were re-extracted without binning and initial 3D refinements were performed against 70S 3D class average maps to determine optimized particle coordinates and 3D orientations. 70S (m¹A1408) datasets were then subjected to focused 3D classification using masks generated from the A-, P-, and E-site tRNA chains of PDB code 5JTE⁴⁰. Classes containing A- and P-site tRNAs were combined for further processing. Datasets were then subjected to iterative CTF refinement³⁶, Bayesian particle polishing⁴¹, and 3D refinement steps to improve map quality. Finally, 70S (A1408) particles were 3D-classified without alignment and without a mask to resolve differences in 30S head domain position before performing final 3D refinement on particles with unrathected 30S subunits and unswept 30S head domains. After final 3D refinement, angular distribution plots were generated using Angdist (v1.2)⁴².

Postprocessing and map sharpening. Following final 3D refinement, maps were postprocessed in RELION-3.1 using solvent masks generated from 10 Å low-pass filtered 3D refinement consensus maps. No sharpening B factor was applied during postprocessing. Local resolution was estimated using the local resolution estimation tool in RELION-3.1. Masked, unsharpened maps from RELION-3.1 were sharpened in PHENIX using the Autosharpen tool⁴³ before use in molecular modeling.

Molecular modeling. PDB code 5JTE⁴⁰ and the tRNA^{fMet} and ribosomal protein L31 chains of PDB code 7K00⁴⁴ were used as starting models. Initial coordinates and geometric restraints for Abk and G418 were generated using PHENIX eLBOW⁴⁵. Models were rigidly fit into the final 3D refinement maps in UCSF ChimeraX⁴⁶ before performing real-space refinement in PHENIX. Local real-space refinement of models was performed as necessary in COOT⁴⁷. Final validation of cryo-EM maps and models was performed in PHENIX using MolProbity⁴⁸.

Summaries of the complete cryo-EM workflow for each complex, as well as all data collection, processing and final model statistics, are provided in Supplementary Figs. 1–4 and Supplementary Table 2. Atomic coordinates and maps were deposited in the Protein Data Bank (PDB) and Electron Microscopy Data Bank (EMDB), respectively (Supplementary Table 2). Helical parameters for h44 A-site nucleotides were calculated using the 3DNA 2.0 webserver⁴⁹.

MD simulations

Simulated systems. Three different systems were generated to simulate the dynamics of aminoglycoside binding to unmodified and m¹A1408-modified rRNA. To assess the potential contributions and interactions between the canonical and secondary h44 aminoglycoside binding sites identified in our cryo-EM structures, two systems were constructed from our structures containing Abk. **System 1** was derived from the 70S (m¹A1408)-Abk complex and included three segments of 16S rRNA (chain AA residues 884–928, 1399–1424, and 1476–1531), an adjacent segment of 23S rRNA nucleotides (chain BA residues 1906–1987), protein S12 (chain AL residues 14–124), A- and

P-site tRNAs (chains AW and AX respectively) and mRNA (chain AV). **System 2** was derived from the 70S (A1408)-Abk complex and contained the same rRNA and protein regions but lacked tRNA and mRNA. Finally, for simulations of canonical site-aminoglycoside interaction, **System 3** comprised a 25-nucleotide A-site RNA model fragment (nucleotides G1486-U1498 and C1403-U1414), with A1492 and A1493 in a “flipped out” configuration. RNA-bound aminoglycoside conformations were taken from experimental structures where available: with an A-site model rRNA for Kan (PDB code 2ESI), Tob (PDB code 1LC4), Amk (PDB code 4P20), Gen (PDB code 2ET3), Par (PDB code 1J7T), and Neo (PDB code 2ET4), and from a 70S ribosomal structure for Plz (PDB code 7LH5). In the absence of an experimental structure, additional aminoglycosides were modeled based on their closest analog: Dbk using Tob (PDB code 1LC4), Mcr using Gen (PDB code 2ET3), and Net using the sisomicin-A-site model RNA complex (PDB code 4F8V).

System preparation and restraints. All system preparation and MD simulations were carried out using the Desmond module of the Schrödinger software suite with the OPLS4 force field⁵⁰. For System 1, methylation at A1408 was computationally removed to generate a corresponding unmethylated version of this system to enable simulation of Abk bound to the canonical and/or secondary sites in the unmethylated state. System 2 was used only in the unmethylated state as derived directly from the original structural coordinates. For System 3 methylated A-site rRNA fragments (m¹A1408 or m⁷G1405), the methyl group was added and a positive charge was assigned to the relevant nitrogen atom (N1 or N7, respectively). Additionally, aminoglycosides were protonated in all simulations, as established by previous MD studies²⁴ and NMR analyses²³. Structure preparation, including the addition of hydrogens, bond order assignment, energy minimization, and hydrogen bond optimization, was performed in Schrödinger. The rRNA-aminoglycoside complex was solvated using TIP3P water molecules with a NaCl concentration of 100 mM. Similarly, for free aminoglycoside simulations, the systems were solvated with a final salt concentration of 100 mM NaCl.

To make the simulations computationally feasible while preserving essential structural context, we employed a “restrained ribosomal section approach” for Systems 1 and 2, in which specific contiguous regions of the ribosome were isolated and restraints were applied to peripheral atoms to mimic the constraints imposed by surrounding residues. Importantly, the h44 site of interest and its associated Abk ligand(s) were left fully unrestrained to allow unbiased sampling of local dynamics. Specifically, a global positional restraint (force constant $k = 0.5$ kcal/mol/Å²) was applied to the system to allow moderate flexibility, except for h44 residues 1402–1420, 1480–1500, and the bound Abk molecule(s), which were unrestrained (force constant $k = 0$ kcal/mol/Å²).

To determine the optimal parameters for System 3, initial simulations of the unmethylated RNA-Kan complex were first run for 100 ns with the RNA restrained using force constant $k = 0, 0.1, 0.2$, or 0.5 kcal/mol/Å², while the aminoglycoside remained fully unrestrained in all cases. Without RNA restraints ($k = 0$ kcal/mol/Å²), root mean square fluctuations (RMSF) of residues A1492, A1493 exceeded 10 Å, indicating unrealistic dynamics. The lowest ($k = 0.1$ kcal/mol/Å²) and highest restraint ($k = 0.5$ kcal/mol/Å²) resulted in high and low RMSF, respectively, with the particularly low values around nucleotides known to be more dynamic (A1492, A1493, and A1408) in the latter case, suggesting this system also did not accurately reflect the system dynamics. A force constant of $k = 0.2$ kcal/mol/Å² for the rRNA was therefore empirically selected for all subsequent simulations using System 3, as the optimal balance of limiting unrealistic RNA flexibility while also capturing relevant dynamics of the rRNA-drug complexes. Finally, as for Systems 1 and 2, all subsequent MD simulations in System 3 and those of free aminoglycosides were performed with no restraint applied to the aminoglycoside, allowing full conformational flexibility.

MD simulation production run and trajectory analysis. All MD simulations were preceded by the default Desmond relaxation protocol to ensure proper equilibration. This protocol begins with a steepest descent minimization (up to 2000 steps or until the energy gradient falls below 25 kcal/mol/Å), followed by a series of restrained simulations: (1) a 12 ps NVT simulation at 10 K with force restraints ($k = 50$ kcal/mol/Å²) on solute heavy atoms using a Berendsen thermostat; (2) a 12 ps NPT simulation at 10 K and 1 atm with the same restraints using a Berendsen thermostat and barostat; (3) a 24 ps NPT simulation at 300 K and 1 atm with restraints on solute heavy atoms; (4) a 24 ps NPT simulation at 300 K and 1 atm with restraints only on solute backbone atoms; and (5) a 240 ps unrestrained NPT simulation at 300 K and 1 atm using a Nose–Hoover thermostat and Martyna–Tobias–Klein barostat. Each system was subsequently equilibrated in the isobaric–isothermal (NPT) ensemble ($P = 1$ atm, $T = 310.5$ K) for 10 ns. Production simulations (100 ns) were then conducted in the NPT ensemble using the final configuration from the equilibration phase. The Langevin thermostat and barostat were employed with relaxation times of 1 ps and 2 ps, respectively. The equations of motion were integrated with multiple time steps: 2 fs for short-range interactions and 6 fs for long-range interactions, applying a 9-Å cutoff for non-bonded interactions. Coordinates were saved every 100 ps. All simulations in Systems 1–3 were performed in triplicate for a cumulative time of 300 ns. Free aminoglycoside simulations were performed as a single production run of 100 ns, which was sufficient to fully sample conformational space. Post-simulation analyses included calculations of RMSD, RMSF, potential energy of the rRNA–aminoglycoside complex, interaction counts, and measurements of aminoglycoside dihedral angles and distances between atoms of aminoglycosides and RNA. The quality of the simulations was evaluated using the Desmond simulation quality analysis module. The convergence of potential energy was confirmed, showing low standard deviations. Additionally, the temperature remained stable throughout the simulations, and the RMSD of the ligand stayed within 2 Å, indicating reliable system stability and simulation quality.

REST simulations. REST simulations were conducted for select aminoglycoside–rRNA complexes using System 3 in Desmond over a total simulation time of 100 ns across 8 parallel replicas, with temperatures ranging from 300 to 410 K. RNA atoms were restrained with a force constant of $k = 0.2$ kcal/mol/Å², as before. Periodic exchanges of configurations between replicas were performed to enhance sampling efficiency. Exchange acceptance ratios ranged from 15% to 20%, with convergence assessed by monitoring potential energy. The simulations otherwise followed the standard Desmond protocol using the OPLS4 force field, and trajectories were analyzed to examine dihedral angle changes and conformational adjustments within the RNA–aminoglycoside complex.

Dihedral angle potential energy scans. To evaluate how the potential energy of each aminoglycoside varies as a function of specific dihedral angles, calculations were performed using the Conformational Scan module in the Schrödinger suite. These calculations were carried out in implicit water with the OPLS4 force field. A conformational scan was conducted by sampling dihedral angles at 10° intervals, capturing a wide range of potential conformations for each aminoglycoside. The potential energy corresponding to specific aminoglycoside dihedral angles was calculated using 500 iterations of steepest descent minimization at each sampled angle. This iterative process ensured that the system converged to a stable local minimum for each conformation. A comparative energy approach was employed, allowing us to evaluate and compare the relative energies of different aminoglycosides, rather than focusing on absolute energy values.

MM-GBSA. Molecular Mechanics Generalized Born Surface Area (MM-GBSA) calculations were performed on a representative structure from the top cluster of each MD simulation replicate, selected based on the aminoglycoside RMSD. Schrödinger's Prime MM-GBSA module was used, with minimization applied only to polar hydrogens to maintain the conformations of both RNA and aminoglycosides during the calculations. Ligand strain energy was calculated from the Prime MM-GBSA results, following previously established procedures^{51,52}.

Reporting summary

Further information on research design is available in the Nature Portfolio Reporting Summary linked to this article.

Data availability

The data supporting the findings of this study are available from the corresponding authors upon request. Atomic coordinates and maps were deposited in the Protein Data Bank (PDB) and Electron Microscopy Data Bank (EMDB), respectively: 70S (A1408)–Abk, PDB 9B50 and EMD 44193, 70S (m¹A1408)–Abk, PDB 9B4Z and EMD 44192, and 70S (m¹A1408)–G418, PDB 9B51 and EMD 44194. Corresponding image datasets were also deposited in EMPIAR: EMPIAR-12843, EMPIAR-12842, and EMPIAR-12844. Source data are provided with this paper.

References

1. Becker, B. & Cooper, M. A. Aminoglycoside antibiotics in the 21st century. *ACS Chem. Biol.* **8**, 105–115 (2013).
2. Krause, K. M., Serio, A. W., Kane, T. R. & Connolly, L. E. Aminoglycosides: an overview. *Cold Spring Harb. Perspect. Med.* <https://doi.org/10.1101/cshperspect.a027029> (2016).
3. Safi, K. H., Damiani, J. M., Sturza, J. & Nasr, S. Z. Extended-interval aminoglycoside use in cystic fibrosis exacerbation in children and young adults: a prospective quality improvement project. *Glob. Pediatr. Health* **3**, 2333794X16635464 (2016).
4. Ratjen, F., Brockhaus, F. & Angyalosi, G. Aminoglycoside therapy against *Pseudomonas aeruginosa* in cystic fibrosis: a review. *J. Cyst. Fibros.* **8**, 361–369 (2009).
5. Jiang, M., Karasawa, T. & Steyger, P. S. Aminoglycoside-induced cochleotoxicity: a review. *Front. Cell Neurosci.* **11**, 308 (2017).
6. Jospe-Kaufman, M., Siomin, L. & Fridman, M. The relationship between the structure and toxicity of aminoglycoside antibiotics. *Bioorg. Med. Chem. Lett.* **30**, 127218 (2020).
7. Serio, A. W., Keepers, T., Andrews, L. & Krause, K. M. Aminoglycoside revival: review of a historically important class of antimicrobials undergoing rejuvenation. *EcoSal Plus*. <https://doi.org/10.1128/ecosalplus.ESP-0002-2018> (2018).
8. Doi, Y. & Arakawa, Y. 16S ribosomal RNA methylation: emerging resistance mechanism against aminoglycosides. *Clin. Infect. Dis.* **45**, 88–94 (2007).
9. Ramirez, M. S. & Tolmasky, M. E. Aminoglycoside modifying enzymes. *Drug Resist. Updat.* **13**, 151–171 (2010).
10. Wachino, J. I., Doi, Y. & Arakawa, Y. Aminoglycoside resistance: updates with a focus on acquired 16S ribosomal RNA methyltransferases. *Infect. Dis. Clin. North Am.* **34**, 887–902 (2020).
11. Seupt, A., Schniederjans, M., Tomasch, J. & Haussler, S. Expression of the MexXY aminoglycoside efflux pump and presence of an aminoglycoside-modifying enzyme in clinical *Pseudomonas aeruginosa* isolates are highly correlated. *Antimicrob. Agents Chemother.* <https://doi.org/10.1128/AAC.01166-20> (2020).
12. Nosrati, M. et al. Functionally critical residues in the aminoglycoside resistance-associated methyltransferase RmtC play distinct roles in 30S substrate recognition. *J. Biol. Chem.* **294**, 17642–17653 (2019).
13. Wachino, J. et al. Novel plasmid-mediated 16S rRNA m¹A1408 methyltransferase, NpmA, found in a clinically isolated *Escherichia*

- coli* strain resistant to structurally diverse aminoglycosides. *Antimicrob. Agents Chemother.* **51**, 4401–4409 (2007).
14. Clark, J. A. & Burgess, D. S. Plazomicin: a new aminoglycoside in the fight against antimicrobial resistance. *Ther. Adv. Infect. Dis.* **7**, 2049936120952604 (2020).
 15. Gur, D. et al. Comparative in vitro activity of plazomicin and older aminoglycosides against Enterobacterales isolates; prevalence of aminoglycoside modifying enzymes and 16S rRNA methyltransferases. *Diagn. Microbiol. Infect. Dis.* **97**, 115092 (2020).
 16. Dunkle, J. A. et al. Molecular recognition and modification of the 30S ribosome by the aminoglycoside-resistance methyltransferase NpmA. *Proc. Natl. Acad. Sci. USA* **111**, 6275–6280 (2014).
 17. Rahman, M. et al. RmtC and RmtF 16S rRNA methyltransferase in NDM-1-producing *Pseudomonas aeruginosa*. *Emerg. Infect. Dis.* **21**, 2059–2062 (2015).
 18. Gamal, D. et al. Carbapenem-resistant *Klebsiella pneumoniae* isolates from Egypt containing blaNDM-1 on IncR plasmids and its association with rmtF. *Int. J. Infect. Dis.* **43**, 17–20 (2016).
 19. Savic, M., Lovric, J., Tomic, T. I., Vasiljevic, B. & Conn, G. L. Determination of the target nucleosides for members of two families of 16S rRNA methyltransferases that confer resistance to partially overlapping groups of aminoglycoside antibiotics. *Nucleic Acids Res.* **37**, 5420–5431 (2009).
 20. Kawai, A., Suzuki, M., Tsukamoto, K., Minato, Y. & Doi, Y. Functional and structural characterization of acquired 16S rRNA methyltransferase NpmB1 conferring pan-aminoglycoside resistance. *Antimicrob. Agents Chemother.* **65**, e0100921 (2021).
 21. Kanazawa, H., Baba, F., Koganei, M. & Kondo, J. A structural basis for the antibiotic resistance conferred by an N1-methylation of A1408 in 16S rRNA. *Nucleic Acids Res.* **45**, 12529–12535 (2017).
 22. Tomono, J. et al. Direct visualization of ribosomes in the cell-free system revealed the functional evolution of aminoglycoside. *J. Biochem.* **175**, 587–598 (2024).
 23. Corzana, F. et al. The pattern of distribution of amino groups modulates the structure and dynamics of natural aminoglycosides: implications for RNA recognition. *J. Am. Chem. Soc.* **129**, 2849–2865 (2007).
 24. Chyzy, P., Kulik, M., Re, S., Sugita, Y. & Trylska, J. Mutations of N1 Riboswitch affect its dynamics and recognition by neomycin through conformational selection. *Front. Mol. Biosci.* **8**, 633130 (2021).
 25. Blanchard, L. S. et al. Multicenter clinical evaluation of ETEST plazomicin (PLZ) for susceptibility testing of Enterobacterales. *J. Clin. Microbiol.* **60**, e0183121 (2022).
 26. Castanheira, M. et al. In vitro activity of plazomicin against Gram-negative and Gram-positive isolates collected from U.S. hospitals and comparative activities of aminoglycosides against carbapenem-resistant Enterobacteriaceae and isolates carrying carbapenemase genes. *Antimicrob. Agents Chemother.* <https://doi.org/10.1128/AAC.00313-18> (2018).
 27. Seely, S. M. et al. Molecular basis of the pleiotropic effects by the antibiotic amikacin on the ribosome. *Nat. Commun.* **14**, 4666 (2023).
 28. Wu, K. J. Y. et al. An antibiotic preorganized for ribosomal binding overcomes antimicrobial resistance. *Science* **383**, 721–726 (2024).
 29. Asensio, J. L. et al. Experimental evidence for the existence of non-exo-anomeric conformations in branched oligosaccharides: NMR analysis of the structure and dynamics of aminoglycosides of the neomycin family. *Chemistry* **8**, 5228–5240 (2002).
 30. Majumdar, S., Parajuli, N. P., Ge, X. & Sanyal, S. Structure-function comparison of Arbekacin with other aminoglycosides elucidates its higher potency as bacterial translation inhibitor. *Sci. Rep.* **15**, 18271 (2025).
 31. Parajuli, N. P., Mandava, C. S., Pavlov, M. Y. & Sanyal, S. Mechanistic insights into translation inhibition by aminoglycoside antibiotic arbekacin. *Nucleic Acids Res.* **49**, 6880–6892 (2021).
 32. Macmaster, R., Zelinskaya, N., Savic, M., Rankin, C. R. & Conn, G. L. Structural insights into the function of aminoglycoside-resistance A1408 16S rRNA methyltransferases from antibiotic-producing and human pathogenic bacteria. *Nucleic Acids Res.* **38**, 7791–7799 (2010).
 33. Witek, M. A. & Conn, G. L. Expansion of the aminoglycoside-resistance 16S rRNA (m¹A1408) methyltransferase family: expression and functional characterization of four hypothetical enzymes of diverse bacterial origin. *Biochim. Biophys. Acta* **1844**, 1648–1655 (2014).
 34. Hong, S. et al. Mechanism of tRNA-mediated +1 ribosomal frame-shifting. *Proc. Natl. Acad. Sci. USA* **115**, 11226–11231 (2018).
 35. Nguyen, H. A., Hoffer, E. D. & Dunham, C. M. Importance of a tRNA anticodon loop modification and a conserved, noncanonical anticodon stem pairing in tRNACGGProfor decoding. *J. Biol. Chem.* **294**, 5281–5291 (2019).
 36. Zivanov, J. et al. New tools for automated high-resolution cryo-EM structure determination in RELION-3. *Elife*. <https://doi.org/10.7554/eLife.42166> (2018).
 37. Zhang, K. Gctf: real-time CTF determination and correction. *J. Struct. Biol.* **193**, 1–12 (2016).
 38. Bepler, T. et al. Positive-unlabeled convolutional neural networks for particle picking in cryo-electron micrographs. *Nat. Methods* **16**, 1153–1160 (2019).
 39. Punjani, A., Rubinstein, J. L., Fleet, D. J. & Brubaker, M. A. cryoSPARC: algorithms for rapid unsupervised cryo-EM structure determination. *Nat. Methods* **14**, 290–296 (2017).
 40. Arenz, S. et al. A combined cryo-EM and molecular dynamics approach reveals the mechanism of ErmBL-mediated translation arrest. *Nat. Commun.* **7**, 12026 (2016).
 41. Zivanov, J., Nakane, T. & Scheres, S. H. W. Estimation of high-order aberrations and anisotropic magnification from cryo-EM data sets in RELION-3.1. *IUCrJ* **7**, 253–267 (2020).
 42. Gaullier, G. angdist: plot the 2D histogram of Euler angles covered by a set of cryo-EM particles (v1.2). Zenodo <https://doi.org/10.5281/zenodo.4104053> (2020).
 43. Liebschner, D. et al. Macromolecular structure determination using X-rays, neutrons and electrons: recent developments in Phenix. *Acta Crystallogr. D Struct. Biol.* **75**, 861–877 (2019).
 44. Watson, Z. L. et al. Structure of the bacterial ribosome at 2 Å resolution. *Elife*. <https://doi.org/10.7554/eLife.60482> (2020).
 45. Moriarty, N. W., Grosse-Kunstleve, R. W. & Adams, P. D. electronic Ligand Builder and Optimization Workbench (eLBOW): a tool for ligand coordinate and restraint generation. *Acta Crystallogr. D Biol. Crystallogr.* **65**, 1074–1080 (2009).
 46. Goddard, T. D. et al. UCSF ChimeraX: meeting modern challenges in visualization and analysis. *Protein Sci.* **27**, 14–25 (2018).
 47. Emsley, P. & Cowtan, K. Coot: model-building tools for molecular graphics. *Acta Crystallogr. D Biol. Crystallogr.* **60**, 2126–2132 (2004).
 48. Williams, C. J. et al. MolProbity: more and better reference data for improved all-atom structure validation. *Protein Sci.* **27**, 293–315 (2018).
 49. Li, S., Olson, W. K. & Lu, X. J. Web 3DNA 2.0 for the analysis, visualization, and modeling of 3D nucleic acid structures. *Nucleic Acids Res.* **47**, W26–W34 (2019).
 50. Lu, C. et al. OPLS4: improving force field accuracy on challenging regimes of chemical space. *J. Chem. Theory Comput.* **17**, 4291–4300 (2021).
 51. Dey, D., Ramakumar, S. & Conn, G. L. Targeted redesign of suramin analogs for novel antimicrobial lead development. *J. Chem. Inf. Model.* **61**, 4442–4454 (2021).

52. Kavanaugh, L. G., Mahoney, A. R., Dey, D., Wuest, W. M. & Conn, G. L. Di-berberine conjugates as chemical probes of *Pseudomonas aeruginosa* MexXY-OprM efflux function and inhibition. *NPJ Anti-microb. Resist.* **1**, 12 (2023).

Acknowledgements

This work was supported by NIH/NIAID award R01 AI088025 (to C.M.D. and G.L.C.) and NIH/NIGMS award T32 GM135060 (to J.M.M.). C.M.D. is a Burroughs-Wellcome Fund Investigator in the Pathogenesis of Infectious Disease. Some of this work was performed at the NCCAT and the Simons Electron Microscopy Center located at the New York Structural Biology Center, supported by the NIH Common Fund Transformative High Resolution Cryo-Electron Microscopy program (U24 GM129539) and by grants from the Simons Foundation (SF349247) and NY State Assembly.

Author contributions

D.D., J.M.M., C.M.D., and G.L.C. designed research; D.D., J.M.M., and N.Z. performed research; D.D., J.M.M., and G.L.C. analyzed data; and D.D., J.M.M., C.M.D., and G.L.C. wrote the paper. D.D. and J.M.M. contributed equally as co-first authors. C.M.D. and G.L.C. are co-corresponding authors.

Competing interests

The authors declare no competing interests.

Additional information

Supplementary information The online version contains supplementary material available at <https://doi.org/10.1038/s41467-025-63278-5>.

Correspondence and requests for materials should be addressed to Christine M. Dunham or Graeme L. Conn.

Peer review information *Nature Communications* thanks Ahmad Jomaa and the other anonymous reviewer(s) for their contribution to the peer review of this work. A peer review file is available.

Reprints and permissions information is available at <http://www.nature.com/reprints>

Publisher's Note Springer Nature remains neutral with regard to jurisdictional claims in published maps and institutional affiliations.

Open Access This article is licensed under a Creative Commons Attribution-NonCommercial-NoDerivatives 4.0 International License, which permits any non-commercial use, sharing, distribution and reproduction in any medium or format, as long as you give appropriate credit to the original author(s) and the source, provide a link to the Creative Commons licence, and indicate if you modified the licensed material. You do not have permission under this licence to share adapted material derived from this article or parts of it. The images or other third party material in this article are included in the article's Creative Commons licence, unless indicated otherwise in a credit line to the material. If material is not included in the article's Creative Commons licence and your intended use is not permitted by statutory regulation or exceeds the permitted use, you will need to obtain permission directly from the copyright holder. To view a copy of this licence, visit <http://creativecommons.org/licenses/by-nc-nd/4.0/>.

© The Author(s) 2025